Perfectly Subcritical Gravity Currents

by

Mitchel S. Baker

A thesis submitted in partial fulfillment of the requirements for the degree of

Master of Science

Department of Mechanical Engineering
University of Alberta

Abstract

This thesis describes an investigation of gravity currents, which are buoyancy-driven horizontal fluid flows. In particular this work reports upon a series of laboratory experiments and complementary (two-dimensional) direct numerical simulations that explore the lock release of a fixed volume of dense fluid into a two-layer density-stratified ambient. By initial condition, the lock release experiments/simulations fall into one of two categories: full-depth and partial-depth. The particular focus of this thesis is on the "tailwaters" limiting case where the lock fluid density matches that of the lower ambient layer. For either initial condition the front speed of the advancing lock fluid (which is termed the "internal front") is less than that of the excited interfacial disturbances. Consequently, the internal front propagates at constant speed for less time than other features of the flow, e.g. the downstream-propagating interfacial disturbance, which is termed the dense gravity current (or GC1). Complementing GC1, there is an analogue flow of light ambient fluid into the lock, and this is referred to as the light gravity current (or GC2). Measured speeds for GC1, GC2, and the internal front are compared against analogue predictions from two-layer shallow water (SW) theory as well as a Yih-type energy analysis (C.-S. Yih. *Dynamics of Nonhomogeneous Fluids.* MacMillan Co., New York, 1965). From this comparison, positive agreement is noted in the case of GC1 and the internal front. Meanwhile, the speed of GC2 post reflection from the lock end wall is under-predicted by 10-20% depending on the initial depth of dense fluid within the lock. This under-prediction is believed to result from a mismatch between where the SW prediction is made (immediately following GC2 reflection from the back of the lock) and where the experimental GC2 speed is measured, usually 0.5-2.5 lock lengths downstream by which point the GC2 height has decreased due to dispersion. Although the GC1 height also undergoes a dispersive decrease in height, generally more positive agreement is noted when comparing measured and predicted gravity current heights. The distance travelled by the internal front prior to being arrested by the reflected GC2 agrees robustly with SW theory. Laboratory and DNS experiments exhibiting a thick ambient interface are also reported upon. It is observed that the speed of the internal front and the downstream distance it travels at a constant speed increase with interface thickness. A second Yih-type analysis of internal front speed is performed in case of thick interfaces, and its predictions agree well with the experimental data.

Preface

Some of the research conducted for this thesis forms part of an international research collaboration led by my supervisor Dr. Morris Flynn at the University of Alberta. The shallow water theory described in Chapter 2 was developed by our collaborator Dr. Marius Ungarish of Technion – the Israel Institute of Technology. I used Dr. Ungarish's theory and solution techniques to produce predictions for the speed, height, and distance measurements obtained from the laboratory and numerical simulations described in Chapter 4. Dr. Flynn conducted all of the numerical simulations while I performed all of the laboratory experiments. I post-processed and analyzed all of the data from the laboratory experiments and numerical simulations. The Yih-type analyses described in Chapter 3 were my original work following a suggestion by Dr. Flynn. The remainder of this thesis was written by me with many helpful edits contributed by Dr. Flynn. In turn, we expect to submit the work described herein for publication in *Environmental Fluid Mechanics*, a leading journal in the field.

Acknowledgments

Thank you, first and foremost, to my wife Jane for letting me take time out of my regular working life to pursue this master's degree. Thank you also to my parents and children for their love and support.

I am greatly indebted to Morris Flynn, my supervisor, for both in my undergraduate and my graduate education in fluid mechanics. In addition to imparting invaluable knowledge and advice, Morris provided steady and clear-eyed guidance that made for a very enjoyable degree. Thank you Morris; your example is inspiring.

Many thanks are also due to Marius Ungarish, our collaborator, for sharing his extensive knowledge of gravity currents and their analysis with shallow water theory, and for his many helpful suggestions and advice.

Thank you to the members of my examining committee, Bruce Sutherland and Jaime Wong. I am also grateful to Bruce for sharing his laboratory space with Morris and his support in performing the laboratory experiments described in this thesis. Bruce was always willing to provide friendly advice and lend us his equipment when needed. Additional thanks to Alain Gervais for his help in formatting this thesis.

Finally, thank you to Shuo and Bharath, my officemates, and to the rest of Morris's research group. It has been a pleasure working with you over these past two years.

Funding for this study was generously provided by the Natural Sciences and Engineering Council of Canada (NSERC).

Contents

List of Tables

List of Figures

Symbols and Abbreviations

Symbol/Abbreviation	Meaning
a	$\frac{h_{Ni}}{H}$
b	$\frac{h_{Ti}}{H}$
c_+,c_-	Speed of the characteristics used in SW model solutions
δ	Interface thickness
DNS	Direct numerical simulation
η_i	GCi height i.e. height of the nose above the tongue
GCi	Gravity current
g'	Reduced gravity, $g\frac{\rho_1-\rho_2}{\rho_1}$
h	Height of the ρ_1 fluid, used especially in the SW model derivation
h_{core}	Height of the ρ_1 fluid located between the GC1 and GC2 fronts
h_{0i}	Initial depth of the fluid reservoirs
h_{initial_i}	Fluid height representing the initial condition in the solution of the shallow water equation (2.3)
h_{Ni}	Height of the gravity current nose above the tank bottom
h_{Ti}	Initial depth of the fluid tongues
H	Total channel depth
i	Subscript for dense fluid ($i = 1$) and light fluid ($i = 2$)
KE	Kinetic energy
l_i	Length of the reservoir (which is the lock length when $i = 1$)
p	Pressure
PE	Potential energy
Plot symbols (open)	Data from numerical experiments
Plot symbols (closed)	Data from laboratory experiments
ρ_i	Fluid density
S	$\frac{\rho_{\text{lower ambient layer}}-\rho_{\text{upper ambient layer}}}{\rho_{\text{dense lock fluid}}-\rho_{\text{upper ambient layer}}}$
SW	Shallow water (theory/model)

continued on next page

continued from previous page

Symbol/Abbreviation	Meaning
U	Speed of the internal front
u	Horizontal speed of the ρ_1 fluid, used espeicially in the SW model derivation
u_{core}	Speed of the ρ_1 fluid between the GC1 and GC2 fronts
u_{initial_i}	Initial fluid speed representing the initial condition in the solution of the shallow water equation (2.3)
u_{Ni}	Speed of the fluid immediately behind the GCi nose
V_{Ni}	Speed of the GCi nose
w	Vertical speed of the ρ_1 fluid, used espeicially in the SW model derivation
x	Horizontal distance from the lock gate (into channel)
x_D	Distance travelled by the internal front prior to its arrest
z	Vertical distance measured from the bottom of the channel

Chapter 1

Introduction

1.1 Background

Density differences strongly influence the dynamics of both the atmosphere and bodies of water. Air density varies due to changing pressure, temperature, and moisture content while oceanic density is influenced by water temperature and salinity. When density decreases continually with height, or when a layer of less dense fluid lies above a dense fluid layer, the fluid is stable and tends to remain stratified. In the opposite case, when density increases with height, the fluid is unstable and convection occurs. All weather, for example, occurs in the lowest layer of the atmosphere, the troposphere, which is heated from below as the sun's radiation warms the Earth's surface. Conversely, in the overlying stratosphere, temperature increases with height, and the tropopause, which is the boundary between the troposphere and the stratosphere, acts as a lid and prevents cloud formation. In an environmental context, density differences give rise to buoyant plumes from smokestacks, influence the dispersion of smog in an urban airshed, and govern the seasonal turnover of lakes (Patterson et al., 1984).

Differences in density can also result in horizontal fluid motion called gravity currents. Gravity currents are ubiquitous in both the natural and industrial world (Simpson, 1999). Gravity currents are present on many scales; atmospheric examples include frontal weather systems, diurnal mountain winds, and airflows present in the heating and cooling of buildings; in the hydrological context, examples are the leading edge of ocean currents, saline wedges in river estuaries, and pipe discharge in a marine environment. There are also multiphase gravity currents such as snow-laden air in avalanches.

In many cases gravity currents propagate through density-stratified, rather than uniform, environments. The density stratification may be discrete, as is the case when the upper layer of a cold body of water is heated by the sun and mixed by wind, or continuous, which often occurs with increasing altitude in the troposphere.

The theoretical analysis of gravity currents dates back nearly 80 years to work by von Kármán (1940), although the problem was first rigorously analyzed in the seminal work of Benjamin (1968). Benjamin considered an air cavity propagating horizontally during the emptying of a long channel containing fluid of uniform density as an analogue to a gravity current. In this steady-state problem, Benjamin transformed the frame of reference to one where the leading edge of the cavity is stationary. Along with continuity considerations, Benjamin hypothesized that the flow force, i.e. the sum of static and dynamic pressure integrated over the cross-section of the container, would be conserved between a point far upstream and one far downstream of the gravity current front. This led to a relationship between gravity current height and speed, which in the special case of an energy-conserving flow, predicts that the gravity current will occupy half the height of the channel and travel at one half of the long wave speed, i.e. Froude number $(Fr = \frac{c_1}{\sqrt{gH}}) = 0.5$. Here, c_1 is the speed of the cavity front, g is the acceleration of gravity, and H is the height of the channel. In the more general case where the gravity current dissipates energy, Benjamin's theory predicts a maximum non-dimensional speed of $\mathrm{Fr} = 0.53$, which occurs at the point where head loss is also a maximum, corresponding to a gravity current height approximately $1/3$ of the channel height. The theory also predicts that gravity currents of height greater than half of the channel height are impossible unless energy is added to the system from an external source.

Huppert & Simpson (1980) derived an empirical relationship between gravity current height and speed based on a series of lock-release experiments (with uniformly-dense ambient fluid) that they performed. This relationship is

$$Fr = \frac{1}{2}\phi^{-\frac{1}{3}} \qquad (0.075 \leq \phi < 1) \tag{1.1}$$

$$Fr = 1.19 \qquad (\phi \leq 0.075) \tag{1.2}$$

where $\phi = h/H$, i.e. the fractional current depth, and the Froude number is given in the same way as defined by Benjamin (1968). They surmise that the former relationship occurs during an initial "slumping" flow, where the forward-propagating disturbance produced as a result of reflection from the back of the lock has not yet overtaken the gravity current front. Meanwhile, the latter relationship pertains to a later self-similar phase when the buoyancy forces are balanced by inertia. Huppert and Simpson's model makes good predictions during these two phases, but deviates from experimental results for large times when viscosity dominates as the force balancing buoyancy. While the empirical relationship agrees qualitatively with Benjamin's theory, it predicts Froude numbers 10-20% lower than those predicted by the analysis of Benjamin.

Rottman & Simpson (1983) present further lock-release experiments where the gravity current propagates into an ambient fluid of uniform density. They compare their experimental data to a two-layer shallow water theory, which is a simplification of the full Navier-Stokes governing equations. Here, by a scaling argument where the length of the channel is much greater than its height, vertical accelerations are much smaller than horizontal accelerations, and the two momentum equations (x and z) are combined into a single horizontal shallow water momentum equation. Rottman and Simpson present a new, two-layer shallow water theory and obtain solutions using numerical methods. In contrast to previously-presented steady-state analyses, the shallow water solutions explicitly apply to time-dependent, lock-release scenarios. Using their experimental data and shallow water theory, Rottman and Simpson argue that the transition from the slumping phase to the inertial-buoyancy phase occurs when the disturbance reflected from the back of the lock overtakes the gravity current. Evidence also supports the idea of a later transition to a phase when viscous effects become important.

A more complicated problem involves gravity currents propagating into ambient environments of two or more layers, distinguished by density. Holyer & Huppert (1980) first performed a theoretical investigation of the two-layer case. Holyer and Huppert's analysis proceeds using the Bernoulli equation several times, mass continuity, and conservation of flow force following the method of Benjamin (1968). They find that, in contrast to Benjamin's single-layer theory, multiple solutions are possible for a given set of parameters. They propose that the solution which occurs in practice is that with the maximum volume of the inflowing gravity current (for energy-conserving solutions), and that where energy loss is at a maximum (for dissipative solutions).

A phenomenon related to gravity currents in multi-layered ambients is the propagation of internal bores along the ambient interface. In an investigation of internal bores propagating in two-layered ambients, Wood & Simpson (1984) performed lock-release experiments and elaborated on a flow-force steady state theory that assumes that the energy is dissipated entirely in the lower, expanding layer. However, this assumption leads to a problematic prediction of an infinite gravity current speed in the limit that the lower ambient layer height $\to 0$, which contradicts Benjamin's accepted prediction of finite speed in this case. Klemp et al. (1997), by contrast, obtained a prediction of finite speed in the the limit of a vanishing lower layer depth by assuming that the dissipation occurs entirely in the upper, contracting layer. Meanwhile, Wood and Simpson's experimental data agrees with the Klemp et al.'s new theory.

More recently, Tan et al. (2011) performed both laboratory and numerical experiments where dense lock fluid was released into a two-layer stratified ambient fluid. They extend Benjamin's analysis to the two-layer case, and obtain closure of the steady state equations using a simple parametrization of height of the deflected ambient interface that is supported by experimental data. This analysis considers both dissipation in the upper ambient layer, and separately, dissipation in the lower ambient layer. Surprisingly, both cases produce similar predictions. Tan et al.'s experimental data showed positive agreement with their theoretical analysis, with a constant offset that is similar to that observed by e.g. Huppert & Simpson (1980). Tan et al. also performed laboratory and numerical lock-release experiments with thick ambient interfaces and found either no change in gravity current speed for various interfaces thickness, or a slight increase in speed with increasing interface thickness depending on initial conditions.

When the ambient fluid is multi-layered, in addition to propagating either along the top or bottom boundaries of the channel, a gravity current may instead advance along the interface between the two ambient layers when it is termed "intrusive". This possibility was first considered by Holyer & Huppert (1980), and intrusive gravity currents now form a broad area of research in their own right, with later investigations by e.g. Sutherland et al. (2004) and Flynn et al. (2008).

1.2 Motivation

This investigation focuses on gravity currents formed by lock-release propagating along the bottom of a two-layer stratified ambient fluid. In the present lock-release context, much attention has been given to *supercritical* gravity currents. Consistent with the definition suggested by Tan et al. (2011), a supercritical gravity current is defined as one whose speed of propagation is larger than that of any long waves or bores that may be excited along the ambient interface as a result of the forcing imparted by the advancing gravity current. As such, and although supercritical gravity currents generate an interfacial disturbance that appears above the gravity current head, this disturbance cannot propagate ahead of the gravity current in the downstream direction.

Conversely, when the gravity current is *subcritical* its frontal speed is comparatively slow and the interfacial disturbance can propagate downstream in the form of a wave or a bore. In this case there may arise a resonant interaction between the current and disturbance (Maxworthy et al., 2002; Tan et al., 2011). Due to this complication, subcritical gravity currents have been less thoroughly investigated. Notable exceptions are the studies by Flynn, Ungarish & Tan (2012) and White & Helfrich (2012). These authors investigated gravity current flow in two-layer stratified ambients for a range of values of the density parameter $S = \frac{\rho_1 - \rho_2}{\rho_c - \rho_2}$, including the subcritical range, which nominally arises for $0.75 \simeq S \leq 1.00$. Here ρ_c is the density of the gravity current while ρ_1 and ρ_2 are the densities of the lower and upper ambient layers, respectively. The analysis of Flynn et al. (2012) proceeds along two parallel tracks. First, they generalize the analysis of Benjamin (1968) and thereby derive a front condition pertinent to the case of a density-stratified ambient. The resulting equations, based as they are on mass and momentum balance, typically admit multiple solutions, one of which is always subcritical. To model the time-dependent lock release problem, Flynn et al. (2012) develop a one-layer shallow water (SW) theory. By combining this SW theory with the semi-empirical front condition suggested by Huppert & Simpson (1980), Flynn et al. (2012) find good agreement with measurements of the gravity current front speed derived from analogue laboratory and numerical experiments. By contrast, White & Helfrich (2012) extend the two-layer hydraulic analysis of Holyer & Huppert (1980) by developing a theory linking upstream bores to the steadily-propagating gravity current front. This yields a resonant band of parameters where upstream undular bores are formed. The resonant band is qualitatively and quantitatively corroborated by data from a large number of lock-release numerical simulations that White & Helfrich (2012) performed. The numerical data falls into regimes corresponding to a vanishing rate of energy dissipation, suggesting that the frontal dissipation is in all cases small.

Although both of the above investigations feature theory and experiments that include subcritical gravity currents, neither especially pays attention to the “perfectly” subcritical case when $S = 1$. This $S = 1$ limit represents the exclusive focus of the present study wherein we perform laboratory and 2D numerical lock-release experiments, and elaborate on the two-layer SW theory of Ungarish (2009) and Ungarish et al. (2014), whose connection to the present work is outlined below. In contrast to Flynn et al. (2012) and White & Helfrich (2012), our theoretical treatment ignores the steady-state problem and instead emphasizes the time-dependent lock-release flows described by our SW model.

Because of our focus on the perfectly subcritical regime where the density of the gravity current matches the density of the lower ambient layer into which it is propagating, we propose a certain change of terminology from that used in studies focusing on gravity current flow with $S \leq 1$. Because the perfectly subcritical gravity current propagates through a layer of equal density, it seems more appropriate to label the leading edge of this flow as an internal front. (Whether in laboratory or numerical experiments, the dense lock fluid and the internal front can be visualized using a passive tracer.) In turn, and consistent with the study of Ungarish et al. (2014), we shall refer to the downstream interfacial disturbance as a gravity current (or, more precisely, GC1), a terminology that becomes more and more appropriate as the depth, h_{T1}, of the lower ambient layer decreases. In a symmetrical fashion, we shall refer to the upstream propagating disturbance (whether or not the initial height of dense lock fluid, h_{01} equals the channel height, H) as a second gravity current, GC2. GC1 thereby issues from Reservoir 1 and flows into a tailwater layer that we will refer to as Tongue 1. (The depth of Tongue 1 is, as noted above, h_{T1}.) Meanwhile, GC2 issues from Reservoir 2 (whose depth is $h_{02} = H - h_{T1}$) and flows into a tailwater that we will refer to as Tongue 2. The depth of Tongue 2 is $h_{T2} = H - h_{01}$ where $h_{T2} = 0$ in the full-depth lock release case. Note finally that GC2 reflects from the lock end wall and thereafter propagates in the downstream direction following the internal front and GC1.

For a schematic summary of the above details, geometrical and otherwise, see figure 1.1. In this schematic, densities are represented by ρ while the boxed variables U and V represent the speed of the internal front and GC fronts respectively, and the other parameters all have dimensions of length. An additional parameter that is not shown in the definition sketch is δ, the thickness of the ambient interface. In figure 1.1, δ is vanishingly small, however, we report upon experiments below where δ is allowed to assume a finite value, i.e. $\delta \leq H$. By contrast, we always assume the density interface inside of the lock to be sharp.

Above, we describe the similarity of terminology with the earlier study of Ungarish et al. (2014). Indeed, Ungarish et al. (2014) likewise examines (using SW theory and numerical simulations) gravity current flow into a tailwater layer. However, there are a number of aspects of this previous study that did not receive complete attention and which we intend to examine here. More especially, in our experiments we distinguish between the lock fluid and the lower ambient layer; the leading boundary between these two is what we refer to above as the internal front, and we consider both the internal front speed and the downstream distance travelled by the internal front before the onset of deceleration. In theory and experiments, we also consider GC2, which, after reflecting off the lock wall, propagates downstream and in some cases overtakes and arrests the internal front. Characterizing the dynamics of not only GC1 but also GC2 and the internal front requires not only that previous analyses be revisited, but that they also be expanded in scope. Doing so using a combination of SW modeling and laboratory and 2D numerical simulations is a central aim of this manuscript. Furthermore, and to complement our SW theory, we perform a Yih-type energy analysis (Yih, 1965), which exhibits surprisingly good agreement with the more rigorous SW results.

Another novel aspect of our work is that it considers the impact of a thick ambient interface and thereby makes a connection with previous investigations of gravity current flow in a continuously stratified ambient e.g. Maxworthy et al. (2002). As we will elaborate upon in more quantitative detail below, increasing the interface thickness leads to an increase in the speed and distance travelled by the internal front. In turn, this observation may have particular import if one wishes to characterize the downstream dispersion of a pollutant in a natural water body in which thermal and/or haline stratification applies. Another application of the $S = 1$ gravity current regime includes the analysis of nocturnal thunderstorm winds, where the temperature of the cold outflow wind matches that of a cold ambient layer adjacent to the ground. Fulton et al. (1990) observed solitary wave behaviour in winds from a nocturnal thunderstorm.

The rest of this thesis is organized as follows: Chapter 2 describes the SW model; complementing this analysis, Chapter 3 presents a simple energy-based model motivated by the seminal work of Yih (1965). Chapter 4 describes the laboratory and DNS experiments while Chapter 5 discusses experimental and theoretical results, and Chapter 6 offers a summary and conclusions. Appendix A provides a summary of the laboratory and DNS experimental parameters while Appendix B describes the preparation of the laboratory experiments. Appendix C elaborates on the SW solution methods and Appendix D relates the gravity current shapes predicted by SW theory to the shapes observed in the experiments.

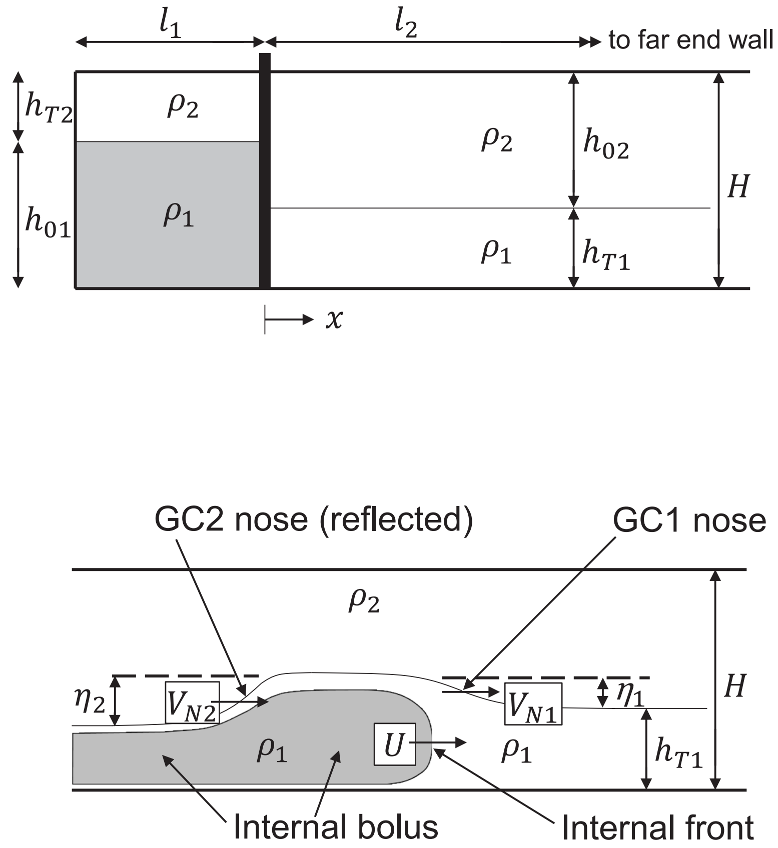

Figure 1.1: Definition sketch for laboratory and numerical experiments showing, in a stationary frame of reference, the initial condition (top) and a snapshot of the flow after the reflection of GC2 from the back of the lock (bottom). Here, the dense fluid from the lock is shaded. Quantities representing speeds are shown in boxes, i.e. U, V_{N1}, and V_{N2}.

Chapter 2

Shallow Water Theory

2.1 Two Layer Governing Equations

The SW model used here follows that of Ungarish and the reader is referred to Ungarish et al. (2014) and Ungarish (2009) for a more in-depth description of the model and its underlying assumptions.

Assuming a 2D rectilinear flow with negligible vertical accelerations, the standard continuity equation is given by

$$\frac{\partial h}{\partial t} + u\frac{\partial h}{\partial x} + h\frac{\partial u}{\partial x} = 0 \tag{2.1}$$

where h is the depth of the fluid having density ρ_1 and u is the corresponding horizontal velocity. The 2D Euler equations can be combined into a single momentum equation because $u \gg w$. Following the analysis of Rottman & Simpson (1983), and applying the Boussinesq approximation leads to

$$\left(\frac{H}{H-h}\right)\frac{\partial u}{\partial t} + \left[\frac{H(H-3h)}{(H-h)^2}\right]u\frac{\partial u}{\partial x} + \left[g' - \left(\frac{H}{H-h}\right)^3\frac{u^2}{H}\right]\frac{\partial h}{\partial x} = 0 \tag{2.2}$$

where x is the horizontal distance from the lock gate, $g' = g\frac{\rho_1-\rho_2}{\rho_1}$ is the reduced gravity, and t is time. The above equations are nondimensionalized by scaling vertical distances with the initial depth of dense fluid inside the lock, h_{01} ($\leq H$), horizontal distances with the lock length, l_1, horizontal velocities with the long wave speed $\sqrt{g' h_{01}}$, and time with $\frac{l_1}{\sqrt{g' h_{01}}}$ (see figure 1.1).

Equations (1) and (2) represent a coupled system of hyperbolic partial differential equations. Applying the method of characteristics (see Ungarish (2009)) results in the following ordinary differential equation:

$$\frac{dh}{du} = \frac{1}{D}\left[Au \mp \sqrt{(Au)^2 + Dh}\right] \tag{2.3}$$

which is valid on characteristic trajectories

$$\frac{dx}{dt} = c_{\pm} = u(1-A) \pm \sqrt{(Au)^2 + Dh} \tag{2.4}$$

Here, $A = \frac{h}{H-h}$, $D = 1 - \frac{h}{H} - \frac{H}{(H-h)^2}u^2$, and variables are now understood to be non-dimensional, a convention that will be maintained until the end of Chapter 2.

2.2 The Nose Condition

While solutions of (2.3) produce a spectrum of h and u, it is still necessary to calculate the behaviour of the gravity current nose, which is the front of the activated fluid. Any fluid beyond the gravity current nose is in the undisturbed initial condition. Additionally, we need a way to relate the speed of the fluid just behind the nose, u_{Ni}, to the speed of the nose V_{Ni}. In figure 1.1, V_{N1} is the speed of GC1 while u_{N1} is the speed of the fluid immediately behind GC1. U is the speed of the internal front, which may be different from u_{N1}. Note that this discussion applies equally to both the dense ($i = 1$) and light ($i = 2$) gravity current.

In many cases the tongue fluid between the internal front and the gravity current nose travels at the same speed u_{N1} as the internal front itself. In other words, and as mentioned in the section 1.2, what defines the internal front (the grey fluid in figure 1.1) is colour (passive tracer) rather than salinity (active tracer).

When there is no dense/light fluid tongue, i.e. $h_{Ti} = 0$, the gravity current front is always a bore which moves at the same speed as the fluid immediately behind it. In this case, and using the non-dimensional variables defined above,

$$u_{Ni} = V_{Ni} = \mathrm{Fr_B}(a)\sqrt{h_{Ni}} \tag{2.5}$$

where h_{Ni} is the height of the nose, $a = \frac{h_{Ni}}{H}$, and $\mathrm{Fr_B}$ is the Froude number function defined by Benjamin (1968)

$$\mathrm{Fr_B}(a) = \sqrt{\frac{(2-a)(1-a)}{1+a}} \tag{2.6}$$

When a fluid tongue is present ($h_{Ti} \neq 0$), the nose behaviour is more complicated. In this case, the GC1 nose is not necessarily a bore; in some cases it may, in fact, be a rarefaction wave. Actually, and as illustrated schematically by figure 2.1, the nose may be one of three types, depending on the height of the tongue h_{Ti}.

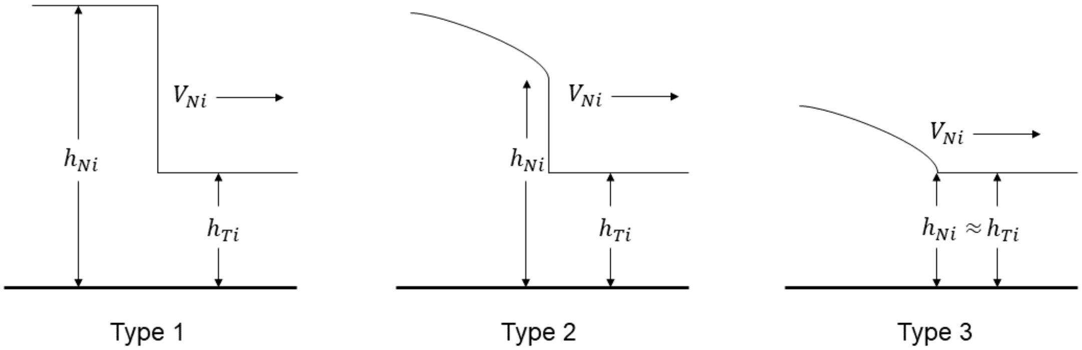

Figure 2.1: An illustration of the three types of nose associated with propagating gravity currents. Type 1 is a bore where the propagation speed is smaller than that of the associated characteristic. Conversely, type 2 and type 3 show, respectively, a bore and a smooth rarefaction wave where, in either case, the speed matches that of the characteristic. Note that $i = 1$ in the case of the bottom, right-propagating gravity current, GC1, and $i = 2$ for the top, left-propagating gravity current, GC2. Schematic adapted from Ungarish et al. (2014).

Following the calculations of Ungarish et al. (2014), the critical tongue thickness for the formation of a type 1 or a type 2 bore reads as

$$\frac{h_{Ti}}{H} < \frac{\sqrt{\rho_1/\rho_2}}{1+\sqrt{\rho_1/\rho_2}} \tag{2.7}$$

which in the Boussinesq limit reduces to $\frac{h_{Ti}}{H} < \frac{1}{2}$. In the case where a bore forms, continuity requires that, in a frame of reference where the bore is stationary, $(u_{Ni} - V_{Ni})h_{Ni} = -V_{Ni}h_{Ti}$. This leads to

$$u_{Ni} = V_{Ni}\left(1 - \frac{h_{Ti}}{h_{Ni}}\right) \tag{2.8}$$

which confirms that the speed of the fluid immediately behind the bore is less than the speed of the bore provided, of course, that $h_{Ti} > 0$. In this case, V_{Ni} no longer depends exclusively on h_{Ni} and H as anticipated by Benjamin (1968) and (2.5). Rather, V_{Ni} is given by

$$V_{Ni} = \mathrm{Fr_T}(a, b)\sqrt{h_{Ni}} \tag{2.9}$$

(Klemp et al., 1997). Here

$$\mathrm{Fr_T}(a, b) = \sqrt{\frac{a(2-a) - b(2-b)}{(a-b)\left(1 + \frac{b}{a} - 2b + 2a\frac{1-b}{1-a}\right)}} \tag{2.10}$$

and $b = \frac{h_{Ti}}{H}$. Note that (2.10) reduces to Benjamin's original formula (2.6) in the limit of a vanishingly thin tongue, i.e. $b \to 0$.

When the gravity current nose is a rarefaction wave (type 3 nose in figure 2.1) (2.9) and (2.10) can be further simplified. After taking the limit $a \to b$, and applying l'Hôpital's rule, it can be shown that

$$V_{Ni} = \sqrt{h_{T1}(1-b)} \tag{2.11}$$

which is the well-known expression for the long wave speed.

2.3 Method of Solution

The solution methods described below were used to solve the SW model for (non-dimensional) values of $H \in [1, 2]$ and $h_{T1} \in [0, 1]$. The solution method begins by solving (2.3) along a characteristic path to determine $u(h)$. The numerical integration requires values for the initial height h_{initial} and speed u_{initial}; specification of these parameters necessitates identification of the nose type for GC1 and GC2.

2.3.1 One Type 3 Nose

The simplest solution arises when either of the gravity currents (GC1 or GC2) has a type 3 nose and so takes the form of a rarefaction wave. When GC2 has a type 3 nose, (2.3) can be solved along a c_+ characteristic that originates at the leading edge of the rarefaction wave. Thus $h_{\text{initial}} = 1$ and $u_{\text{initial}} = 0$ and the solution of (2.3) is obtained for $h \in [1, h_{T1}]$. The so-determined solution of $u(h)$ is then used in (2.4) to calculate the spectrum of characteristics and to verify that the GC1 nose is of type 1. (Note that for the range of parameters of interest here, a type 3 nose was never found to coexist with a type 2 nose.) The GC1 nose speed, V_{N1}, and height, h_{N1}, is then solved using (2.8) and (2.9). See Appendix C for details.

When the opposite is true, i.e. GC1 has a type 3 nose and GC2 has a type 1 nose, (2.3) may instead be integrated along a c_- characteristic considering $h_{\text{initial}} = h_{T1}$ and $u_{\text{initial}} = 0$. The solution of (2.3) is then obtained for $h \in [h_{T1}, 1]$.

2.3.2 No Type 3 Nose

When neither gravity current has a type 3 nose, one may proceed by assuming that both noses are of type 2. (The case when one nose is of type 1 rather than of type 2 will be addressed below.) Then (5.38) from Ungarish (2009), $V_{N2} \simeq 0.1798H + 0.3475$, may be used to calculate the speed and height of both GC1 and GC2. Equation (5.38) is a curve-fit to the speed of a bore propagating into an equal-density tongue as obtained from a two-layer shallow water model, i.e. equations 5.36 and 5.37 from Ungarish (2009). Note that (5.38) may be directly applied to find V_{N2} prior to reflection; however, to find V_{N1}, the "upside down" equivalent to H must be calculated: i.e. the channel height normalized by $H - h_{T1}$. The initial height and speed to be used in solving (2.3) are the height of the bore and the speed of the fluid just behind the bore (i.e. the fluid on the lock gate-side of the bore, which applies to both GC1 and GC2). Equation (2.3) is therefore solved twice, once to calculate $u(h)$ on a c_+ characteristic and once to calculate $u(h)$ on a c_- characteristic. Thus (2.3) is integrated forwards with $h \in [h_{\text{initial}_2}, h_{T1}]$ and backwards with $h \in [h_{\text{initial}_1}, 1]$. The intersection of the so-obtained curves for $u(h)$ specifies the height, h_{core}, and speed, u_{core}, of the fluid in the core section between the two bores. See figure 2.2 for a schematic representation of this SW solution.

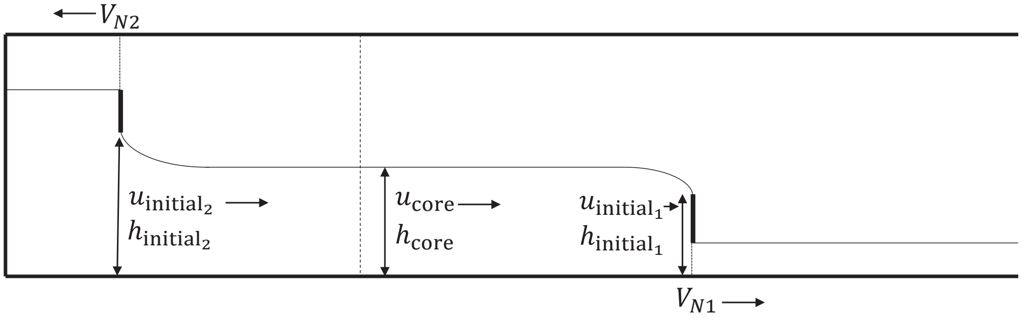

Figure 2.2: Schematic of the SW solution for a lock release experiment where both gravity current noses are type 2 bores. The initial height and speed to be integrated forward along a c_+ characteristic are shown, and are respectively located at and just to the right of the left-moving jump (V_{N2}). The initial height and speed to be integrated backwards along a c_- characteristic are also shown, and are respectively located at and just to the left of the right-moving jump (V_{N1}). Also shown is the position of the lock gate (vertical dashed line) and the height and speed of the core fluid.

Failing to obtain an intersection of the two $u(h)$ curves implies that one (or both) of the GC noses is (are) of type 1. This means that a weaker bore than calculated by (5.38) from Ungarish (2009) must be used to determine h_{initial} and the corresponding u_{initial}. Essentially this can be done by either choosing an h_{initial_2} that is slightly higher or an h_{initial_1} that is slightly lower than that obtained from (5.38), then calculating the appropriate u_{initial_i} by first computing the corresponding bore speed (i.e. V_{N2} or V_{N1}), using (2.9). Thereafter, continuity arguments may be employed e.g. (2.8). Which initial (h, u) pair is to be adjusted is determined by which of the two $u(h)$ curves (first described in the preceeding paragraph) must be extended to yield the desired intersection. The smallest change that achieves an intersection should be made, i.e. h_{initial} (and the corresponding u_{initial}) should be changed just enough to achieve intersection and no more. The final bore speed and height is that which just results in intersecting $u(h)$ curves and, as above, the intersection point of the two curves determines the height and speed of the core fluid between the bores. A graphical method summarizing this process and analogous to that described in Appendix C may be helpful, and is shown in figure C.2 below.

2.3.3 Reflected GC2

The height and speed of GC2 following reflection from the back of the lock are determined using the method of Ungarish (2009), which is briefly outlined below. Here, we assume that GC2 is either a type 1 or type 2 bore. When this is not the case, i.e. GC2 is a type 3 bore, the incident and reflected disturbance will both be rarefaction waves as noted by Rottman & Simpson (1983). We do not examine theoretically this type 3 nose case.

Figure 2.3 shows GC2 immediately following reflection from the back of the lock. The upstream conditions were previously determined using the SW analysis detailed above. Only V_{N2} and h_{N2} are unknown. It is helpful to first introduce the ratio

$$\chi = \frac{h_{N2}}{h_2} \tag{2.12}$$

Continuity yields

$$V_{N2} = -\frac{u_2}{\chi - 1} \tag{2.13}$$

The reduced hydrostatic pressure to the right of the bore is

$$p_r = \begin{cases} h_1 - z & (0 \leq z \leq h_1) \\ 0 & (h_1 \leq z \leq H) \end{cases} \tag{2.14}$$

Changing the frame of reference to one where the bore is stationary allows us to consider the increase in pressure along the top boundary in figure 2.3. Bernoulli's equation gives

$$\frac{1}{2}V_{N2}^2 + p_L + \Delta = \frac{1}{2}(u_2 + V_{N2})^2 \tag{2.15}$$

where Δ denotes the head loss across the bore and p_L is the unknown pressure along the top boundary to the left of the bore. Making the simplifying assumption that $\Delta = 0$ (which shows good agreement with more rigorous calculations (Klemp et al., 1997)) yields

$$p_L = \frac{1}{2}u_2^2 + u_2 V_{N2} \tag{2.16}$$

where u_2 is understood to be a negative quantity. This result allows us to calculate the hydrostatic pressure to the left of the bore:

$$p_l = \begin{cases} p_L + H - h_{N2} - z & (0 \leq z \leq H - h_{N2}) \\ p_L & (H - h_{N2} \leq z \leq H) \end{cases} \tag{2.17}$$

A flow-force balance is then applied on the left and right side of the bore (still in the moving frame of reference) as follows:

$$\int_0^H (u^2 + p)_l dz = \int_0^H (u^2 + p)_r dz \tag{2.18}$$

Substituting (2.12-2.14) and (2.17) into (2.18) ultimately yields:

$$\frac{u_2^2}{\chi - 1} = u_1^2(G - 1) + u_2^2(1 - \frac{1}{2}G) + \frac{1}{2}h_2\{(G-1)^2 - (G - \chi)^2\} \tag{2.19}$$

where $G = H/h_2$. Equation (2.19) represents one equation for one unknown, χ. The height and speed of the reflected GC2 are valid for the conditions in the lock immediately following reflection; if the height and speed of the fluid layers into which the reflected GC2 is propagating change, the height and speed of GC2 will necessarily change as well.

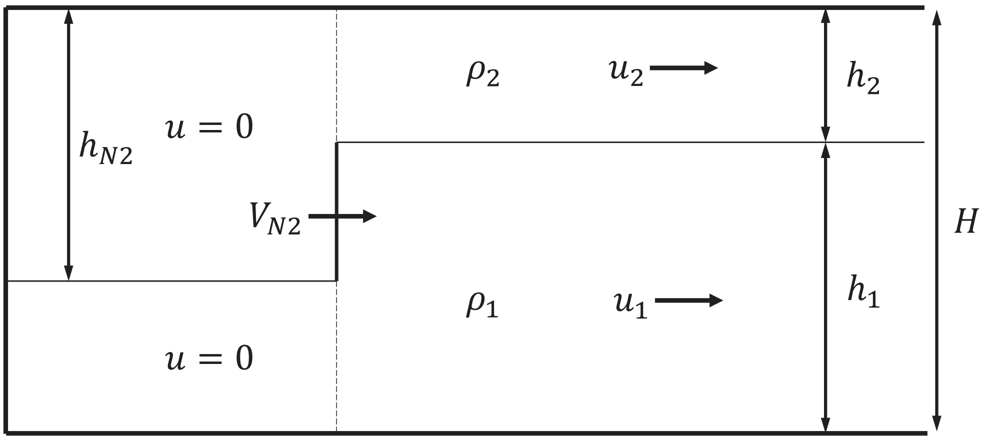

Figure 2.3: Schematic of the SW solution for the reflected GC2 showing the bore shortly after reflection from the back of the lock. u_1, u_2, h_1, and h_2 are known, having been determined in the initial SW analysis. Schematic adapted from figure 5.7 of Ungarish (2009).

Chapter 3

Yih-type Energy Analysis

To complement the results obtained by SW theory, a Yih-type energy analysis (Yih, 1965) is performed for the sole purposes of estimating the internal front speed and the speed of GC1. By design, the analysis is not as comprehensive as that presented in Chapter 2 e.g. it applies only up till the point where GC2 reflects from the end of the lock.

3.1 Thin Interfaces

Figure 3.1 shows the definition sketch for thin interface experiments where, consistent with experimental images to be presented later, we have assumed that the dense lock fluid pushes downstream fluid from the lower ambient layer. GC1 and GC2 are assumed to be type 1 bores linked by a core region of constant thickness, with depth h_{N1} equal to that of the GC1 nose. Strictly speaking, this assumption is inconsistent: for the parameters of interest here, the SW model never actually predicts configurations in which both gravity current noses are type 1 bores. However, and as shown in figure 5.1 below, we find that the Yih-type analysis exhibits surprisingly good accuracy, at least insofar as anticipating the speeds of the internal front and GC1. Rationalizing this observation, we note that, most of the time, the SW model predicts bore pairs in the combinations of type 2-type 2 or type 1-type 2. It is therefore likely that the geometry/energetics of the type 2 bore is sufficiently close to that of a type 1 bore to render a Yih-type analysis an alternative that is neither unreasonable nor computationally expensive. Note that from this section onward variables are once again dimensional.

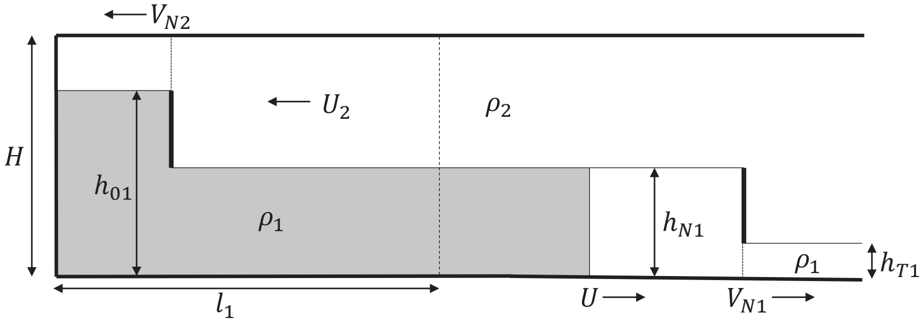

Figure 3.1: Definition sketch for the Yih-type energy-based analysis. Both GC noses are assumed to be type 1 bores. The lock fluid is shaded, and the position of the lock gate before removal is shown as a vertical dashed line. The internal front moves with speed U while the activated region of Tongue 1, whose initial depth is h_{T1}, propagates as a bore with speed $V_{N1} \neq U$.

The analysis proceeds by evaluating the change in potential and kinetic energies that occur between the initial condition and a time Δt after lock release. To evaluate the change in potential energy of fluid 2, a volume centered on the lock gate and having lateral extent $(V_{N1} + V_{N2})\Delta t$ is considered at $t = 0$ and then again at a later instant in time, $t = \Delta t$. With reference to this volume, the change in potential energy of fluid 2 is

$$\Delta PE_{\text{fluid}_2} = \frac{1}{2}\rho_2 g \Delta t \big[V_{N1}(h_{T1}^2 - h_{N1}^2) + V_{N2}(h_{01}^2 - h_{N1}^2)\big] \tag{3.1}$$

Similarly, the potential energy change of fluid 1 during time Δt can be calculated as

$$\Delta PE_{\text{fluid}_1} = \frac{1}{2}\rho_1 g \Delta t \big[V_{N1}(h_{N1}^2 - h_{T1}^2) + V_{N2}(h_{N1}^2 - h_{01}^2)\big] \tag{3.2}$$

The corresponding change in kinetic energy of fluid 1 can be determined by considering the domain of fluid of density ρ_1 activated during Δt, i.e.

$$\Delta KE_{\text{fluid}_1} = \frac{1}{2}\rho_1 \Delta t (V_{N1} + V_{N2}) U^2 h_{N1} \tag{3.3}$$

The analogous expression for fluid 2 is

$$\Delta KE_{\text{fluid}_2} = \frac{1}{2}\rho_2 \Delta t (V_{N1} + V_{N2}) U_2^2 (H - h_{N1}) \tag{3.4}$$

Ignoring viscous dissipation, the sum of (3.1), (3.2), (3.3), and (3.4) must vanish. This observation, combined with the mass balance identities

$$V_{N1} = U\frac{h_{N1}}{h_{N1} - h_{T1}} \qquad V_{N2} = U\frac{h_{N1}}{h_{01} - h_{N1}} \qquad U_2 = U\frac{h_{N1}}{H - h_{N1}} \tag{3.5}$$

leads to the following expression for U:

$$\frac{U^2}{g'H} = \mathrm{Fr}^2 = \left(1 - \frac{h_{N1}}{H}\right)\left(\frac{h_{01}}{H} - \frac{h_{N1}}{H}\right)\left(1 - \frac{h_{T1}}{h_{N1}}\right) \tag{3.6}$$

The height h_{N1} being unknown, we consider the same symmetrical split as was done by Yih (1965). Accordingly $h_{N1} - h_{T1} = h_{01} - h_{N1}$ or, equivalently,

$$\frac{h_{N1}}{H} = \frac{1}{2}\left(\frac{h_{01}}{H} + \frac{h_{T1}}{H}\right) \tag{3.7}$$

Combining (3.6) and (3.7) leads to

$$\frac{U^2}{g'H} = \mathrm{Fr}^2 = \frac{1}{2}\left[1 - \frac{1}{2}\left(\frac{h_{01}}{H} + \frac{h_{T1}}{H}\right)\right]\left(\frac{h_{01}}{H} - \frac{h_{T1}}{H}\right)\left(\frac{h_{01} - h_{T1}}{h_{01} + h_{T1}}\right) \tag{3.8}$$

With an expression for U to hand, V_{N1} can then be estimated from (3.5a).

3.2 Thick Interfaces

Figure 3.2 shows the definition sketch for thick interface experiments where, consistent with experimental images to be presented later, we have assumed that the dense lock fluid pushes downstream fluid from the lower ambient layer. We also assume a linear change in density from ρ_1 to ρ_2 across the thick interface. As in §3.1 above, GC1 and GC2 are assumed to be type 1 bores linked by a core region of constant thickness, with depth h_{N1} equal to that of the GC1 nose. As before, this assumption may be inconsistent, although the previous SW model does not apply to experiments with thick interfaces. A final simplifying assumption is that the activated portion of the thick interface moves to the left at the same speed as the upper ambient layer, V_{N2}. In spite of the above assumptions, we find that the Yih-type analysis exhibits reasonably good accuracy in predicting the speed of the internal front, as shown in figure 5.7 below. This analysis thus provides a straightforward way of predicting the speed of the internal front when the interface is thick and $h_{01} = H$.

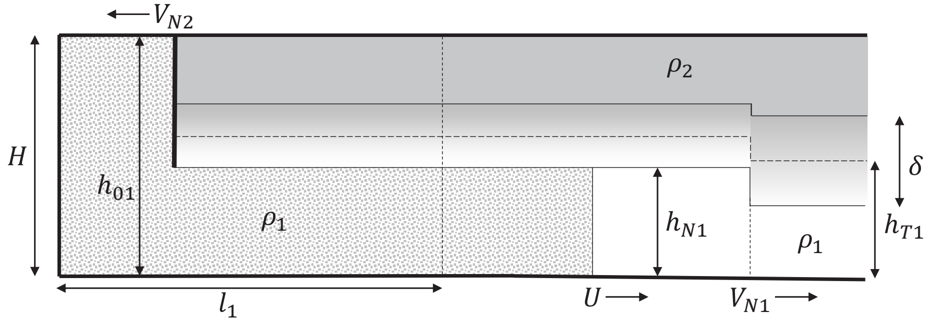

Figure 3.2: Definition sketch for the Yih-type energy-based analysis with a thick ambient interface and where $h_{01} = H$. Both GC noses are assumed to be type 1 bores. The lock fluid is stippled while the light ambient fluid is shaded. The density variation in the thick interface is represented by a colour gradient, and the position of the lock gate before removal is shown as a vertical dashed line. The internal front moves with speed U while the activated region of Tongue 1, whose initial depth is $h_{T1} - \frac{\delta}{2}$, propagates as a bore with speed $V_{N1} \neq U$.

The analysis proceeds by evaluating the change in potential and kinetic energies that occur between the initial condition and a time Δt after lock release. To evaluate the change in potential energy of the fluid in the thick interface, a volume centered on the lock gate and having lateral extent $(V_{N1} + V_{N2})\Delta t$ is considered at $t = 0$ and then again at a later instant in time, $t = \Delta t$. With reference to this volume, the change in potential energy of the thick interface, whose average density is $\frac{1}{2}(\rho_1 + \rho_2)$, is

$$\Delta PE_{\text{interface}} = \frac{1}{2}(\rho_1+\rho_2)g\Delta t V_{N1}\delta\big[h_{N1} + \frac{V_{N1}\delta}{2(V_{N1}+V_{N2})} - h_{T1}\big] \tag{3.9}$$

Similarly, the potential energy change of fluid 1 during time Δt can be calculated as

$$\Delta PE_{\text{fluid}_1} = \frac{1}{2}\rho_1 g\Delta t\big[V_{N1}(h_{N1}^2-(h_{T1}-\delta/2)^2)+V_{N2}(h_{N1}^2-H^2)\big] \tag{3.10}$$

and the potential energy change of fluid 2 during time Δt is

$$\begin{aligned}\Delta PE_{\text{fluid}_2} = {} & \frac{1}{2}\rho_2 g\Delta t V_{N1}\big[H-(h_{T1}+\delta/2)\big] \\ & \left[\frac{V_{N1}}{V_{N1}+V_{N2}}\big[2\delta+H-(h_{T1}+\delta/2)\big]+2h_{N1}-H-(h_{T1}+\delta/2)\right]\end{aligned} \tag{3.11}$$

The corresponding change in kinetic energy of fluid 1 can be determined by considering the domain of fluid of density ρ_1 activated during Δt, i.e.

$$\Delta KE_{\text{fluid}_1} = \frac{1}{2}\rho_1\Delta t(V_{N1}+V_{N2})U^2 h_{N1} \tag{3.12}$$

The analogous expression for fluid 2 is

$$\Delta KE_{\text{fluid}_2} = \frac{1}{2}\rho_2\Delta t(V_{N1}+V_{N2})\frac{H-(h_{T1}+\delta/2)}{H-(h_{T1}-\delta/2)}U^2\frac{h_{N1}^2}{H-h_{N1}} \tag{3.13}$$

while the change in kinetic energy of the thick interface is

$$\Delta KE_{\text{interface}} = \frac{1}{2}\frac{\rho_1+\rho_2}{2}\Delta t(V_{N1}+V_{N2})\frac{\delta}{H-(h_{T1}-\delta/2)}U^2\frac{h_{N1}^2}{H-h_{N1}} \tag{3.14}$$

Ignoring viscous dissipation, the sum of (3.9) – (3.14) must vanish. This observation, combined with the mass balance identities

$$V_{N1} = U\frac{h_{N1}}{h_{N1}-(h_{T1}-\delta/2)} \qquad V_{N2} = U\frac{h_{N1}}{H-h_{N1}} \tag{3.15}$$

yields, after a considerable amount of algebra, the following expression for U:

$$\frac{U^2}{g'H} = \mathrm{Fr}^2 = \frac{\left(1-\frac{h_{N1}}{H}\right)^2\left(1-\frac{h_{T1}}{h_{N1}}+\frac{\delta}{2h_{N1}}\right)\left[\left(\frac{h_{T1}}{H}-1\right)^2+\left(\frac{\delta}{2H}\right)^2\right]}{\left(1-\frac{h_{T1}}{H}+\frac{\delta}{2H}\right)^2} \tag{3.16}$$

The height h_{N1} being unknown, we consider the same symmetrical split as was done by Yih (1965), noting that in the case of a thick interface the lower ambient layer depth is now given by $h_{T1} - \delta/2$. Accordingly $h_{N1} - (h_{T1} - \delta/2) = H - h_{N1}$ or, equivalently,

$$\frac{h_{N1}}{H} = \frac{1}{2}\left(1 + \frac{h_{T1} - \delta/2}{H}\right) \tag{3.17}$$

Note finally that we do not attempt a Yih-type analysis for the case of a thick ambient interface and a partial-depth lock release anticipating that the associated algebraic manipulations will be too complicated to yield a practical solution, not at least without invoking overly restrictive simplifying assumptions.

Chapter 4

Experiments

A total of 43 laboratory and 85 direct numerical simulation (DNS) lock-release experiments were performed. We consider a two-layer density-stratified ambient in all cases although in roughly half of the experiments, the ambient interface was thick and supported a continuous (and roughly linear) variation of ρ with z. In all experiments $H \simeq 20\,\mathrm{cm}$ with $\Delta\rho \simeq 4\%$ in the laboratory experiments and $\Delta\rho = 2\%$ in the DNS experiments. The Reynolds number was defined as $\mathrm{Re} = \frac{\rho_2 U H}{\mu}$ where the dynamic viscosity was taken to be $\mu = 0.01002\,\mathrm{g/(cm{\cdot}s)}$ (Kundu et al., 2012). Although Re varied from approximately 400 to 23 000, the influence of viscosity was small and features of turbulent flow were consistently observed. Parameters that were varied in the thin interface experiments were the depth of the dense lock fluid, h_{01}, in reservoir 1, and the depth, h_{T1}, of tongue 1. For the thick interface experiments, we additionally varied the thickness, δ, of the ambient interface. However, the center of the ambient interface was kept constant at $h_{T1} = 10\,\mathrm{cm}$.

4.1 Laboratory Experiments

Lock-release laboratory experiments were performed in a $227\,\mathrm{cm} \times 25\,\mathrm{cm} \times 34\,\mathrm{cm}$ glass tank having a wall thickness of 1.2 cm. The lock region spanned a horizontal distance of

36 cm at the left end of the tank. The lower and upper ambient layers were respectively comprised of salt water and fresh water, the latter of which was dyed orange with food colouring. Meanwhile, the dense fluid in the lock, whose density matched that of the lower layer, was dyed blue so that the internal front could be easily identified in experimental images. For all laboratory experiments, the depth of the fluid inside the lock was 20.0 cm whereas the depth of the fluid outside of the lock was slightly larger, 20.0 to 20.6 cm. (The fluid inside and outside of the lock were hydrostatically-balanced at $t = 0$.) Parameter combinations with reservoir 1 (dense lock fluid) depth 10 cm $< h_{01} <$ 20 cm and tongue 1 (dense ambient layer) depth 2.5 cm $< h_{T1} <$ 15 cm were used. See Appendix A for a listing of all laboratory experiments. Also, a summary of laboratory experimental preparation techniques is included in Appendix B.

Laboratory experiments were initiated by removing the lock gate as quickly as possible. The speed of the lock gate removal was limited by the tightness of the rubber seals and varied from 9 seconds in experiment 1 to 2 seconds in experiment 43 as the seals became progressively looser with repeated use. Tight seals were necessary to prevent fluid migration, i.e. leakage during the filling process due to hydrostatic pressure differences across the lock gate. The finite time required to remove the lock gate in the laboratory experiments did not, however, impact the bulk features of the flow; this is evident in figures 4.1 and 4.2, which compare time series of images from laboratory experiments with and those from the analogous simulations.

Experimental videos were captured by a tripod-mounted DSLR camera (EOS REbel T5i, Canon) and analyzed using post-processing software (see §4.3 below). The camera, which was aligned with the center of the long side of the experimental tank, was located a sufficient distance away (i.e. 375 cm) to minimize parallax errors. When parallax is defined relative to the total tank length, it varies from zero at the image center to 3% at the outside edges of the tank. The camera's 18-55 mm zoom lens (Canon) was set to a focal length of approximately 35 mm.

Thick interfaces were carefully prepared using one of three methods depending on the required thickness: for thinner interfaces an intrusive gravity current was used, as described in Mehta, Sutherland & Kyba (2002); for medium interfaces a lock exchange technique as elborated upon in Shin et al. (2004) was used; and for thick interfaces Oster's double bucket method (Oster, 1965) was used. In this latter case in particular, ambient density profiles were obtained using a conductivity probe (MSCTI, Precision Measurement and Engineering) that was lowered into the tank on a LabView-controlled traverse. As expected, the measurements in question confirmed that the density varied in a roughly linear fashion from the top of the lower ambient layer to the bottom of the upper ambient layer – see Appendix B for further details.

4.2 Numerical Experiments

Analogous 2D DNS experiments were performed where the numerical domain measured 400 cm × 20 cm, the former distance including a 40 cm lock. A heavy fluid density of $\rho_1 = 1.02\,\mathrm{g/cm^3}$ and a light fluid density of $\rho_2 = 1.00\,\mathrm{g/cm^3}$ were used. A passive tracer was used to keep track of the fluid originating in the lock. Simulations were run using Diablo (Taylor, 2008), an open-source, mixed spectral-finite difference algorithm that employs a staggered grid with spatial resolutions of 0.2 cm and 0.08 cm, respectively, in the horizontal and vertical directions. Diablo, which employs a Runge-Kutta-Wray (RKW3) scheme for time advancement, has been used in numerous previous investigations of gravity current behaviour e.g. Flynn, Boubarne & Linden (2008), Flynn, Ungarish & Tan (2012), Bolster et al. (2008) and Maurer et al. (2010). As with the laboratory experiments described previously, the primary purpose of running the numerical simulations is to examine the bulk features of the fluid flow such as the speeds and heights of the gravity currents as well as the speed of the internal front. These flow dynamics are largely unaffected by turbulent flow detail, the most intense turbulent mixing being observed behind the features of principal interest.

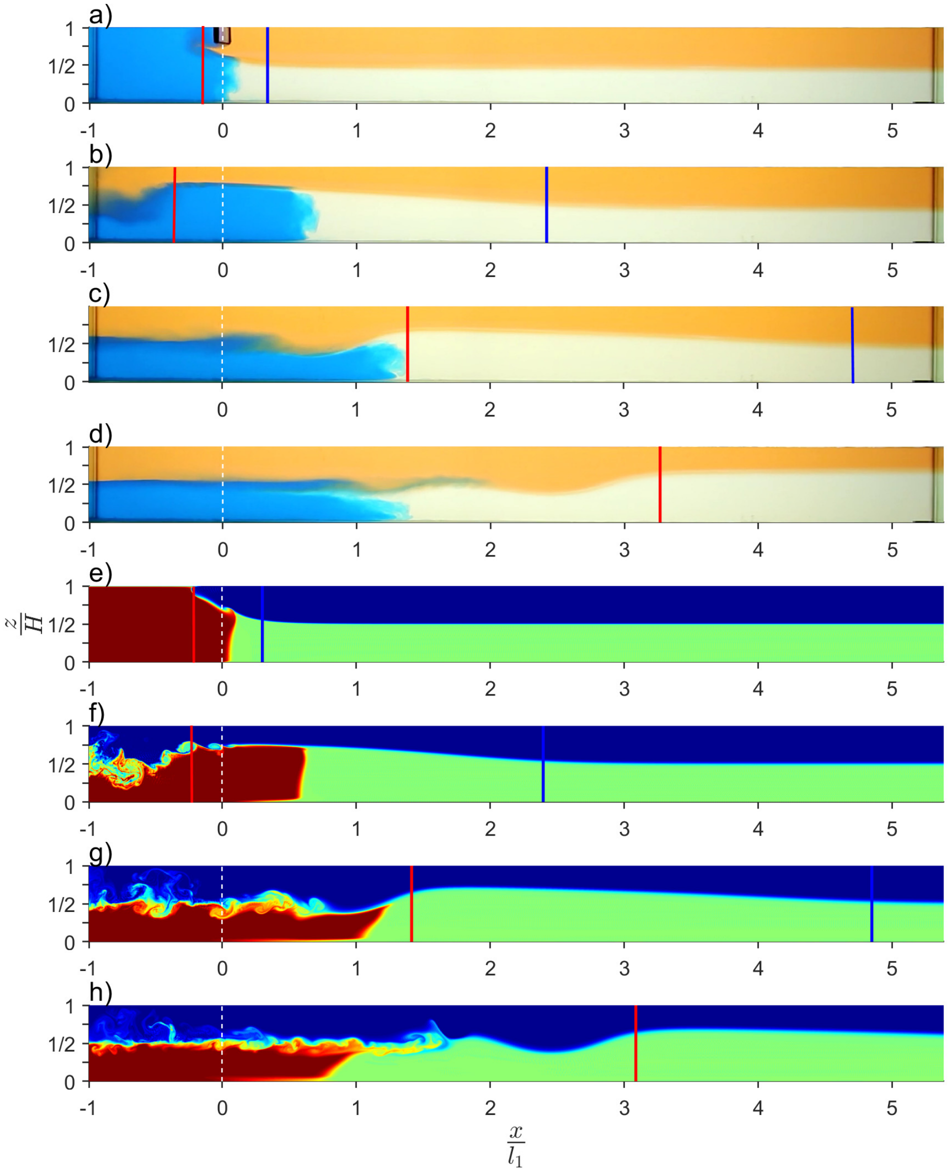

Figure 4.1: Time series of laboratory experiment 1 (panels a-d) and the corresponding DNS experiment 583 (panels e-h) with $\frac{h_{01}}{H} = 1.0$ and $\frac{h_{T1}}{H} = 0.5$. Consistent with the dimensions of our experimental tank, each of the above panels measures 227 cm × 20 cm. The position of the lock gate is indicated by the vertical white dashed line. The frames shown correspond to non-dimensional times $t\frac{\sqrt{g'H}}{H}$ of 2.0 (a and e), 10.0 (b and f), 18.0 (c and g), and 26.0 (d and h) following the initiation of the flow. The vertical blue and red lines respectively denote the nose positions of GC1 and GC2, the latter of which reflects from the back of the lock between panels (a-b) and (e-f).

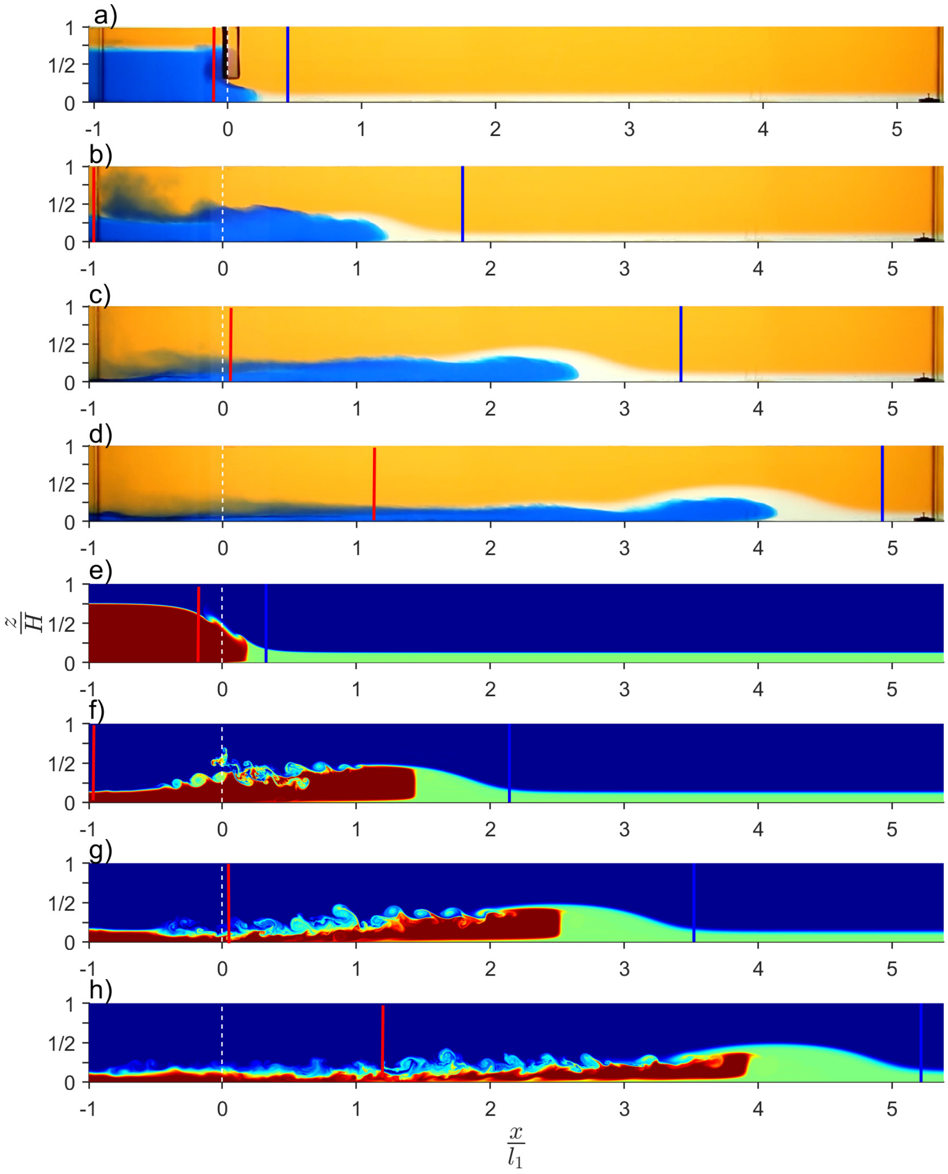

Figure 4.2: Time series of laboratory experiment 10 (panels a-d) and the corresponding DNS experiment 584 (panels e-h) with $\frac{h_{01}}{H} = 0.75$ and $\frac{h_{T1}}{H} = 0.125$. Consistent with the dimensions of our experimental tank, each of the above panels measures 227 cm × 20 cm. The position of the lock gate is indicated by the vertical white dashed line. The frames shown correspond to non-dimensional times $t\frac{\sqrt{g'H}}{H}$ of 2.0 (a and e), 8.0 (b and f), 14.0 (c and g), and 20.0 (d and h) following the initiation of the flow. The vertical blue and red lines respectively denote the nose positions of GC1 and GC2, the latter of which reflects from the back of the lock between panels (a-c) and (e-g).

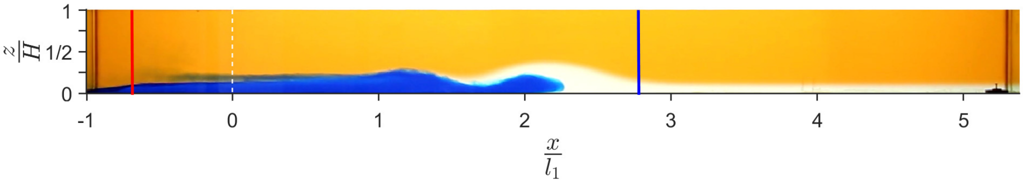

Figure 4.3: Image from laboratory experiment 13 with $\frac{h_{01}}{H} = 0.5$ and $\frac{h_{T1}}{H} = 0.125$. Consistent with the dimensions of our experimental tank the image domain measures 227 cm × 20 cm. The position of the lock gate is indicated by the vertical white dashed line. The frame shown corresponds to a non-dimensional time $t\frac{\sqrt{g'H}}{H}$ of 14.0 following the initiation of the flow. The vertical blue and red lines respectively denote the nose positions of GC1 and GC2, the latter of which has previously reflected from the back of the lock.

Supporting this claim, figures 4.1–4.2 show a comparison of analogue time series images. The former and latter figures respectively consider cases where the GC1 nose is predicted to be of type 3 and type 2. Figure 4.2 justifies the terminology adopted in Chapter 1 whereby the interfacial disturbance generated downstream of the internal bolus is referred to as GC1. As the lock depletes of dense fluid, there is a gradual evolution of GC1 and its type 2 nose, i.e. the bore assumes an undular character. Such behavior is even more evident in figure 4.3, which considers a smaller value of $\frac{h_{01}}{H}$, i.e. 0.5 vs. 0.75 from figure 4.2. The lead solitary wave from the undular bore has a “leaky” core and so includes dense lock fluid in progressively diminishing volumes. Because shallow water models cannot capture such non-hydrostatic effects, the interested reader is instead referred to Sutherland & Nault (2007) where the generation of solitary waves by gravity currents is discussed in greater detail. Together, figures 4.1–4.3 illustrate the different forms that the interfacial disturbances can take, i.e. a long wave, a bore, or a solitary wave. The figures also confirm that the bulk flow features from the laboratory experimental images are faithfully reproduced in the corresponding images extracted from the DNS experiments.

4.3 Post-processing and Analysis

Laboratory experimental videos were cropped and resampled to 12 frames per second to reduce file size, typically resulting in videos comprised of approximately 500 frames. Video frames were then converted into arrays of 8-bit RGB values, with array sizes of roughly 225 × 1600 × 3. Pixel resolution was determined by selecting points a known distance apart in the first video frame.

Typical DNS data consisted of 51 frames of double-precision active and passive scalar values stored in 256 × 2048 arrays. The time increment between successive output files was therefore 1.25 s, however, the actual time step used in the simulations was smaller by a factor of 250.

MATLAB algorithms were used to measure the internal front position as well as the nose position of both gravity currents. The position of the internal front was determined by averaging, row-by-row and across the vertical extent of the tank, the horizontal locations of either a specified RGB colour value (lab) or a passive tracer concentration (DNS). The GC1 front position was measured by executing a five row search along the level of the ambient interface to determine where the interface height first deviated from its downstream value. The GC2 front position was determined using a broadly similar technique to that used to locate the internal front, i.e. by searching for a change in the RGB colour value or passive tracer concentration over the five rows spanning the level approximately ten rows below the crest GC2.

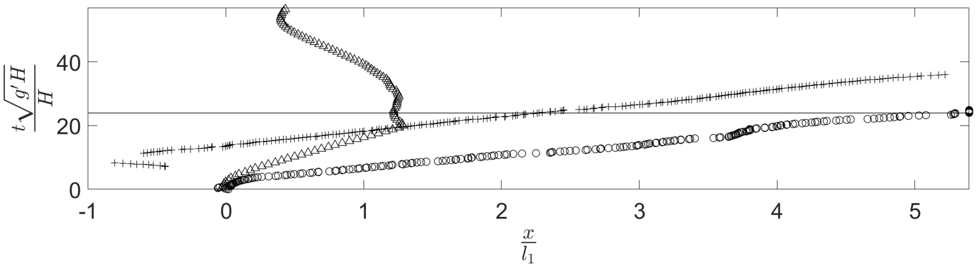

Figure 4.4: Horizontal time series of laboratory experiment 1, with $\frac{h_{01}}{H} = 1$ and $\frac{h_{T1}}{H} = 0.5$. Symbol types are as follows: internal front, triangles; GC1, circles; GC2, crosses. The solid horizontal line represents the time at which GC1 reflects from the tank end wall.

On this basis we were able to produce horizontal time series (HTS) images like the one in figure 4.4. The symbols in figure 4.4 correspond to the data from experiment 1, shown in the top four panels of figure 4.1. Plotted in figure 4.4 are the positions of the internal front (triangles), GC1 nose (circles), and GC2 nose (crosses). In the latter case, we show data from before and after the reflection of GC2 from the back of the lock. The gaps in the GC2 data around the point of reflection are due to the difficulty in measuring its nose position right at the point of reflection, which is oftentimes associated with enhanced shear and mixing.

In figure 4.4, the internal front exhibits a well-defined region of constant-speed propagation that can be observed between non-dimensional times of 0 and 17. Thereafter, the internal front is arrested by the overtaking GC2. The horizontal line indicates the time of reflection of GC1 and confirms that in the case shown, the internal front's arrest was due to the overtaking GC2 rather than the reflection of GC1. There exists a smaller subset of experiments (not shown) where GC2 propagates relatively slowly and/or the internal front travels relatively quickly. Here, the internal front begins to decelerate when it feels the downstream influence of the tank end wall. Indeed such a downstream influence and, more especially, the reflection of GC1 has the eventual consequence of pushing the internal front from right to left after a period of frontal stasis – see figure

4.4. The associated dynamics, being an artifact of our closed/finite domain, are not of particular interest in the context of real environmental flows and shall not be examined in significant detail here. In other words, our research emphasizes the period between lock release and the arrest of the internal front, whether this is due to overtaking by GC2 or to the reflection of GC1. In general, as $\frac{h_{T1}}{H}$ decreases (in thin interface experiments) or as the interface thickness δ increases (in thick interface experiments), the internal front moves more quickly and is able to travel further downstream before its progress is arrested. Additionally, GC1 and GC2 travel at approximately constant speed until they interact with the tank end wall. Also of note is that GC2 travels more quickly when initially moving to the left into the undisturbed lock fluid than after reflecting from the back of the lock and propagating to the right.

The precise front speeds for GC1 and GC2 as well as the speed of advance of the internal front are estimated by drawing lines of best fit to the relevant data over the appropriate time interval. In turn, the distance travelled by the internal front before decelerating was determined as the point where the open triangles from the HTS images first deviated from the corresponding best fit line. Our MATLAB algorithm was further extended to measure gravity current heights (see figure 4.5) in the case of the thin interface experiments. This was done by detecting the border between fluid 1 and fluid 2 by searching for a specified difference in colour (laboratory experiments) or scalar tracer (DNS experiments).

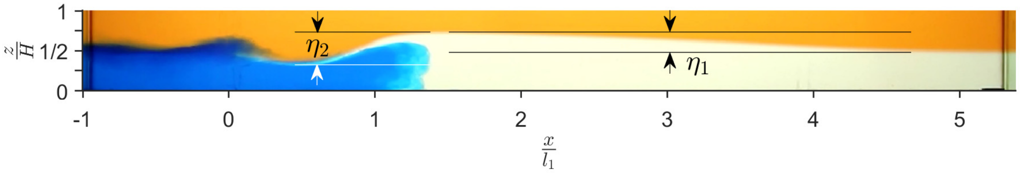

Figure 4.5: Image taken from experiment 7 with $\frac{h_{01}}{H} = 1$ and $\frac{h_{T1}}{H} = 0.5$. The entire tank length of 227 cm × 20 cm is shown. The two pairs of horizontal lines are used to estimate the heights of GC1 and GC2 (reflected).

The height of the detected border was then averaged over a specified range of x, usually about 20 pixels or 4 cm. This range was chosen by eye, and corresponded to the extent of approximately constant gravity current height.

GC1 and GC2 heights were each measured at two locations: The GC1 height was measured both when its leading edge reached two lock lengths, which was as early as practical, and when its leading edge reached the end of the tank, i.e. 5.4 lock lengths. In the case of the numerical simulations, which had a longer horizontal domain, the second GC1 height was nonetheless measured at 5.4 lock lengths, this for the sake of consistency. The GC2 height, by contrast, was measured both immediately following its reflection from the back of the lock, and at the point where the GC2 front overtook the internal front. When the internal front was arrested by interaction with the far tank wall rather than by the overtaking GC2, the second GC2 height was measured as far downstream as possible, before GC1 first contacted the end of the tank.

The prediction of gravity current heights derived from SW theory is based on the assumption of a hydrostatic pressure gradient on either side of the propagating bore. However, when GC2 reflects from the back of the lock, vertical accelerations may result and pressures may become non-hydrostatic. For this reason, the measurement of the GC2 height immediately following reflection required some care. For example, figure 4.6 shows a vertical time series (VTS) taken at the position where the GC2 height was measured, in this case at -0.6 lock lengths. The line indicates the time interval over which the GC2 trough could be measured. Although the height measurement was taken at point in time where pressures were likely non-hydrostatic, the measured trough depth is actually very similar to that corresponding to later times, when vertical accelerations were again small. This gives reasonable confidence that our method for estimating the height of GC2 is accurate.

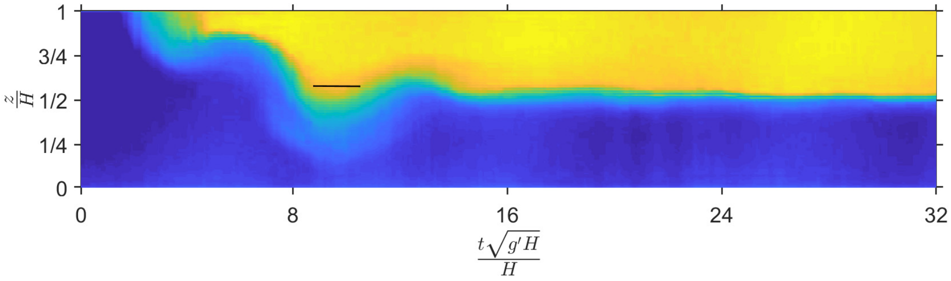

Figure 4.6: Vertical time series of laboratory experiment 1 taken at $\frac{x}{l_1} = -0.6$. Here $\frac{h_{01}}{H} = 1$ and $\frac{h_{T1}}{H} = 0.5$. The blue region represents the lock fluid while the yellow region represents the upper ambient layer. The line indicates the vertical position and range of time that the height of the GC2 trough could be measured immediately following reflection from the back of the lock.

Chapter 5

Results and Discussion

5.1 Thin Interface Experiments

Figure 5.1 shows internal front and gravity current speeds as measured during the period where the internal front speed is constant. Each panel also shows predictions made by SW theory (thick lines) and the Yih-type analysis (thin lines). Regions within each panel of figure 5.1 are shaded according to the GC1 nose type as predicted using SW theory and the equations of §2.2.

In the case of GC1 (open and filled squares, and solid lines), and in good agreement with qualitative observations from experiments, SW theory predicts the appearance of a type 1 or type 2 bore for $\frac{h_{T1}}{H} < 0.5$ and a rarefaction wave for $\frac{h_{T1}}{H} \geq 0.5$ (Ungarish et al., 2014). (The time series in figure 4.1 illustrates a GC1 front at the crossover value of $\frac{h_{T1}}{H} = 0.5$.) The SW prediction for the GC1 speed is nonetheless continuous at $\frac{h_{T1}}{H} = 0.5$ as confirmed by the solid curves of figures 5.1 a-d, which agree well with both laboratory (filled squares) and DNS data (open squares) for the full range of $\frac{h_{T1}}{H}$ values.

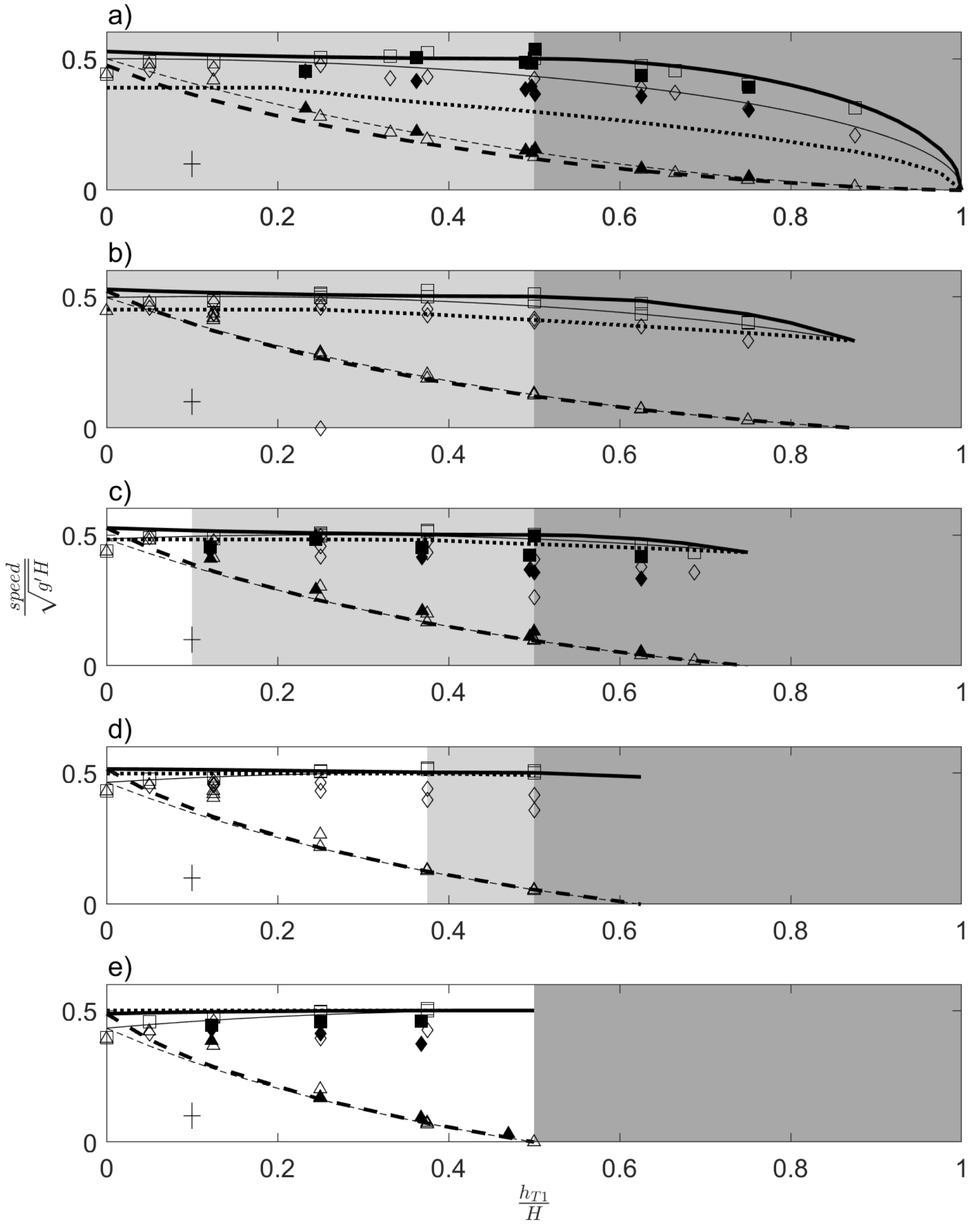

Figure 5.1: Plots of non-dimensional speed versus non-dimensional dense tongue depth for decreasing dense lock fluid depths. The panels show experiments where (from top to bottom) $\frac{h_{01}}{H} = 1.00, 0.88, 0.75, 0.63,$ and 0.50. The panels show GC1 speed (squares and solid lines), reflected GC2 speed (diamonds and dotted line) and internal front speed (triangles and dashed line data) Open symbols represent DNS data while closed symbols represent laboratory experiments. The thick lines are predictions made by SW theory (Chapter 2) while the thin lines are predictions made by the Yih-type analysis (Chapter 3). The background shading shows the GC1 nose type predicted by SW theory, including type 1 (white), type 2 (light grey), and type 3 (dark grey). Representative error bars are as shown.

Turning now to the predictions of the Yih-type analysis for the GC1 speed, there is generally good agreement with both the SW theory and the experimental data when $\frac{h_{T1}}{H} \lesssim 0.5$ or when $\frac{h_{01}}{H} < 1.0$. When $\frac{h_{01}}{H} = 1.0$ and $\frac{h_{T1}}{H} > 0.5$ and, however, the Yih-type analysis under-predicts both the GC1 speed data (open and closed squares in figure 5.1 a) and the SW prediction of the GC1 front speed. This may be because, as noted previously, the Yih-type analysis assumes that GC1 is always a type 1 bore. However, both experimental images and more especially SW theory indicate that when $\frac{h_{T1}}{H} \geq 0.5$, GC1 is instead a rarefaction wave, which here travels faster than a type 1 bore.

Measured internal front speeds are shown in figure 5.1 as open and closed triangles while the corresponding theoretical predictions are given by the thick (SW) and thin (Yih) dashed curves. Both the thick and thin curves approximately approach Benjamin's prediction of $\frac{U}{\sqrt{g'H}} = 0.5$ as $h_{T1} \to 0$ (Benjamin, 1968); they also approach $\frac{U}{\sqrt{g'H}} = 0$ as $h_{T1} \to h_{01}$. In between these extremes, the correspondence between SW/Yih theory and experiments is both robust and roughly comparable to the agreement observed by Tan et al. (2011), whose focus was primarily on supercritical flows and who derived a corresponding theory that was neither SW or Yih-like in nature. It is interesting to note, with reference to the experimental measurements in figure 5.1, that both internal front and GC1 speeds decrease slightly as $\frac{h_{T1}}{H} \to 0$ from the right. We speculate that a thin lower layer may play something of a "lubricating" role that suppresses the overrunning of ambient fluid by GC1. Consider, for example, figure 5.2, which shows snapshots collected from three numerical experiments that are identical in all aspects except for the value of h_{T1}. Although the simulations are 2D, it is clear that $h_{T1} = 0$ is associated with the most significant turbulent mixing behind the gravity current head. In turn, the speed of both GC1 and of the internal front are demonstrably smaller than in the case where $\frac{h_{T1}}{H} = 0.05$ (middle panel).

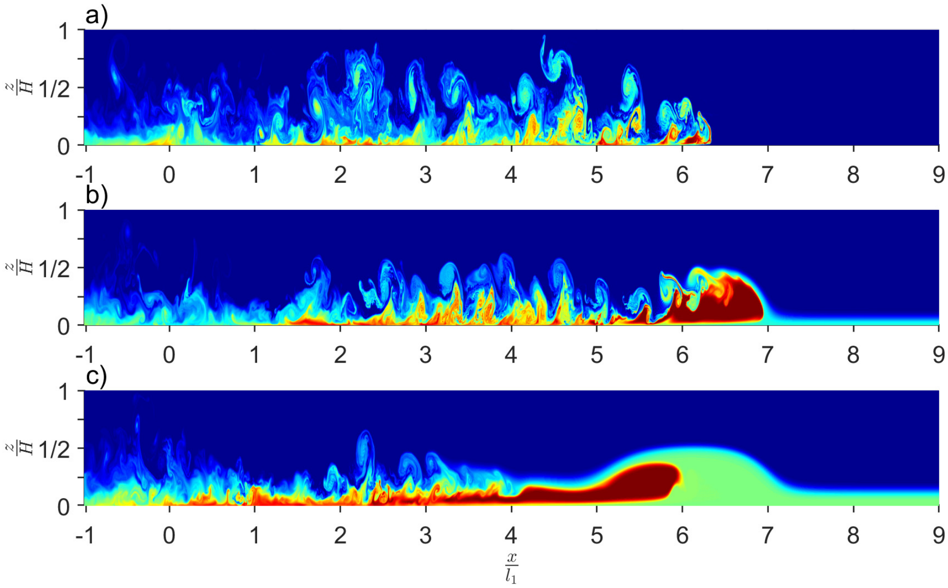

Figure 5.2: Images from DNS experiments 249, 571, and 573 with $\frac{h_{01}}{H} = 1.0$ and initial dense tongue heights $\frac{h_{T1}}{H} = 0.0$ (top), 0.05 (middle), and 0.125 (bottom). The non-dimensional time after lock release is $\frac{t\sqrt{g'H}}{H} = 31$ in all cases. The lock fluid is shown in red, while the lower ambient layer is green and the upper ambient layer is blue. The entire numerical domain of 400 cm × 20 cm is shown.

Comparing the internal front speed predictions of the Yih-type analysis to those of SW theory in figure 5.1, positive agreement is noted for a wide range of $\frac{h_{T1}}{H}$ and for all $\frac{h_{01}}{H}$. When $\frac{h_{01}}{H} \leq 0.75$, and in the limit of $\frac{h_{T1}}{H} \to 0$, however, the Yih-type model underpredicts its SW counterpart. While the Yih-type prediction seems to be consistent with the numerical data points at $\frac{h_{T1}}{H} = 0$, the agreement is likely coincidental. As evidenced by figure 5.2, the reduced speeds seen in the numerical simulations are likely due to the increased turbulent mixing and dissipation that arises when the ambient lower layer is absent. The Yih-type analysis, by contrast, ignores turbulent mixing entirely.

Figure 5.1 also includes data for the reflected GC2 nose (diamonds) and the corresponding SW theory (dotted lines). (We do not attempt to measure the front speed of GC2 before reflection owing to transient effects and the moderate lock lengths of interest here.) The SW theory predicts a bore rather than a rarefaction wave in the top 4 panels where $\frac{h_{01}}{H} = 1.00, 0.88, 0.75$, and 0.63. The bottom panel predicts that the initially left-moving GC2 propagates with a type 3 nose (rarefaction wave) and upon reflection a type 3 nose is also anticipated (Rottman & Simpson, 1983). Overall, the agreement between experiment and theory is here less robust than for GC1 and the internal front, which is especially evident in figure 5.1 a) where a ∼20% underprediction is observed. This may be because SW theory predicts the GC2 speed immediately following reflection from the lock wall. In practice, reflection is associated with such a large degree of mixing that, for pragmatic reasons, measured front speeds for GC2 are more typically collected 0.5 to 2.5 lock lengths downstream of the back wall of the lock, after the bore has reduced in height and increased in speed. This relationship of bore speed to height is predicted by (2.13). In fact, when $\frac{h_{01}}{H} = 1.0$ and the SW prediction for the GC2 front speed is based instead on experimentally-measured heights, which are used as inputs to (2.19) and that are measured at a downstream distance where the GC2 front overtakes the internal front, we see considerable better agreement between theory and experiment – see figure 5.3.

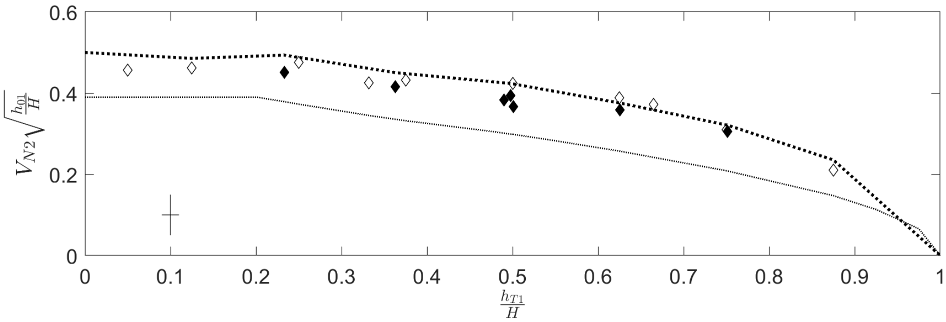

Figure 5.3: Plots of the non-dimensional GC2 front speed versus the non-dimensional dense tongue depth for $\frac{h_{01}}{H} = 1.0$. Shown are reflected GC2 speed experimental data (diamonds) and predictions from SW theory (thin dotted line), both of which are taken from figure 5.1 a. Also included above with the thick dotted line (but not in figure 5.1 a) is an analogue SW prediction made using experimentally-measured heights as inputs to (2.19). Open symbols represent DNS data while closed symbols are data points from laboratory experiments. Representative error bars are as shown.

Evidence for a dispersive evolution of GC2 in the streamwise direction comes from the right-hand side panels of figure 5.4, which plot $\frac{\eta_{2R}}{H}$, the GC2 height immediately following reflection from the back of the lock against $\frac{\eta_{2O}}{H}$, the GC2 height as the GC2 front overtakes the internal front. For $\frac{\eta_{2O}}{H} \gtrsim 0.2$, the GC2 height decreases with distance travelled, as evidenced by the data points lying above the 1:1 line. The parametric range in question corresponds to experiments with relatively low values of $\frac{h_{T1}}{H}$. Indeed when $\frac{h_{T1}}{H}$ is especially small, the time-dependent height decrease in GC2 has the longest time over which to manifest. The left-hand side panels of figure 5.4 plot $\frac{\eta_{2R}}{H}$ against $\frac{h_{T1}}{H}$ (open and filled diamonds). Also included in these panels are the predictions of SW theory (thick lines). The agreement between experiments and theory is excellent in the full-depth case (a) and remains qualitatively correct when $\frac{h_{01}}{H} = 0.75$ (c). No SW prediction is possible when $\frac{h_{01}}{H} = 0.5$, in which case GC2 is predicted to take the form of a long wave rather than a bore.

Complementary results but considering GC1 are shown in figure 5.5, whose left-hand-side panels show $\frac{\eta_{1,2.0}}{H}$, as measured after a travel distance of two lock lengths vs. $\frac{h_{T1}}{H}$. The agreement with SW theory (thick lines) is good, albeit with an underprediction of the DNS data (open squares) when $\frac{h_{T1}}{H} < 0.2$ in panels (c) and (e). Conversely, the right-hand side columns show $\frac{\eta_{1,2.0}}{H}$, versus $\frac{\eta_{1,5.4}}{H}$, GC1 height measured at a downstream distance of 5.4 lock lengths, which corresponds to the far end wall of the laboratory tank. While the full-depth case (b) exhibits a decrease in gravity current height between these two points, the same cannot be said for the $\frac{h_{01}}{H} = 0.75$ and 0.5 data (panels d and f). Here, and within experimental uncertainty, $\eta_{1,2.0}$ remains constant with downstream distance.

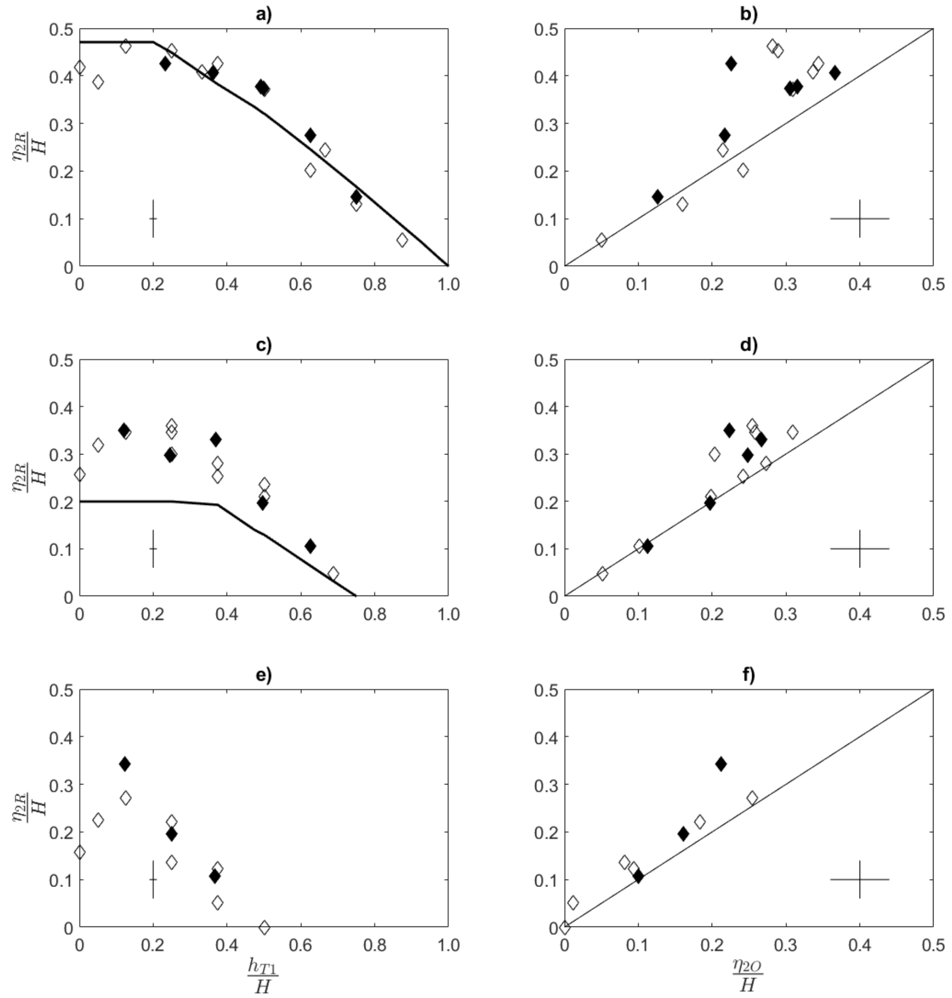

Figure 5.4: Plots of reflected GC2 height immediately following reflection versus dense fluid tongue depth (left column) and reflected GC2 height at the point of overtaking the internal front (or, in those select cases where overtaking was not responsible for decelerating the internal front, at the point where GC1 reached the tank end wall). $\frac{h_{01}}{H} = 1.0$ (top), 0.75 (middle), and 0.5 (bottom). Open symbols are data from DNS experiments whereas closed symbols are laboratory data. The thick lines are predictions of SW theory, while the thin lines represent 1:1 correspondence. Representative error bars are as shown.

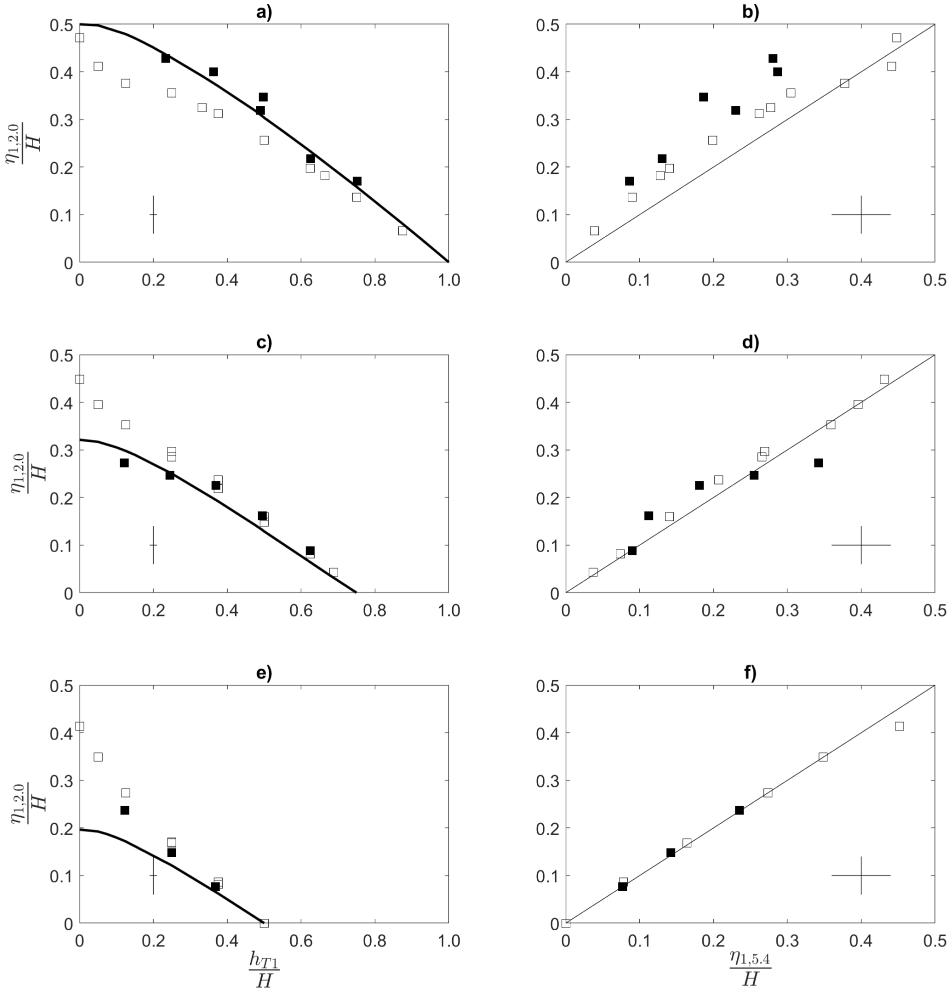

Figure 5.5: Plots of GC1 height measured at two lock lengths versus dense fluid tongue depth (left column) and GC1 height measured at the far end of the tank (right column - 5.4 lock lengths). $\frac{h_{01}}{H} = 1.0$ (top), 0.75 (middle), and 0.5 (bottom). Open symbols are data from DNS experiments whereas closed symbols are laboratory data. The thick lines are predictions of SW theory, while the thin lines represent 1:1 correspondence. Representative error bars are as shown.

Finally, the downstream distance travelled by the internal front before deceleration is plotted against $\frac{h_{T1}}{H}$ in figure 5.6. Here, the agreement between theory and experiment is excellent. In fact, SW theory predicts a rapid increase in the distance travelled as the speed of the internal front approaches the speed of the reflected GC2. In the limit, the reflected GC2 will never catch up to the internal front, and the internal front will propagate long distances at constant speed as has been observed in related contexts by Mehta et al. (2002), Sutherland et al. (2004), and Tan et al. (2011).

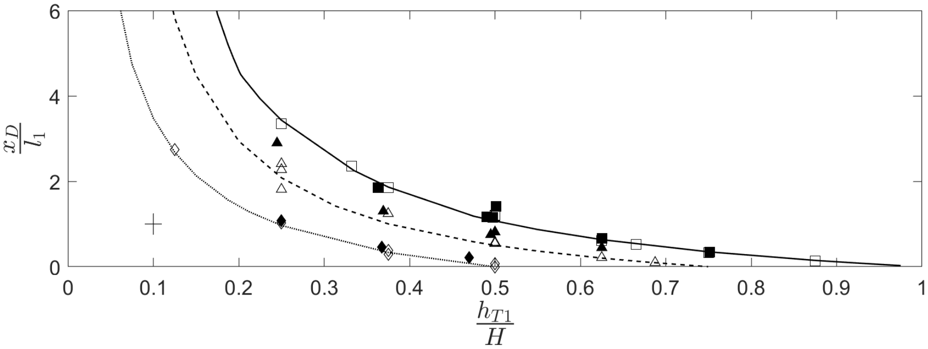

Figure 5.6: Distance of first deceleration of the internal front vs. non-dimensional dense tongue depth. Data and SW theory include squares and a solid line ($\frac{h_{01}}{H} = 1.0$), triangles and a dashed line ($\frac{h_{01}}{H} = 0.75$), and diamonds and a dotted line ($\frac{h_{01}}{H} = 0.5$). Open symbols represent DNS data while closed symbols are data obtained from laboratory experiments. Representative error bars are as shown.

5.2 Thick Interface Experiments

Figure 5.7 shows the variation of internal front speed with interface thickness. In contrast to figure 10 b of Tan et al. (2011), which consider subcritical gravity currents with $S < 1$, here there is a more substantial variation of $\frac{U}{\sqrt{g'H}}$ with $\frac{\delta}{H}$ e.g. an approximate doubling of the front speed as $\frac{\delta}{H}$ increases from 0 to 1 for the case where $\frac{h_{01}}{H} = 1.0$. This can be understood intuitively as follows: when the interface thickness increases for fixed h_{T1}, a progressively thinner lower ambient layer is present. Thus increasing δ is analogous to decreasing h_{T1} and, in either case, we expect a larger internal front speed to result – see e.g. figure 5.1.

Our results, specifically those where $\frac{\delta}{H} = 1$, may also be compared to SW theory and experimental results from the literature. Table 5.1 shows a comparison between our measurements vs. those made by Maxworthy et al. (2002). Also included are the SW predictions of Ungarish & Huppert (2002). Good agreement between the three sets of results is seen.

Table 5.1: $\frac{U}{\sqrt{g'H}}$ vs. $\frac{h_{01}}{H}$ in the limit of a very thick interface, $\frac{\delta}{H} = 1$. Also included are measurements made by Maxworthy et al. (2002) and SW predictions due to Ungarish & Huppert (2002).

$\frac{h_{01}}{H}$	U&H	M et al.	Extrapolated Laboratory Data	Numerical Data
1.00	0.28	0.27	0.28	0.29
0.75	0.23	–	0.27	0.28
0.50	0.17	0.19	0.17	0.20

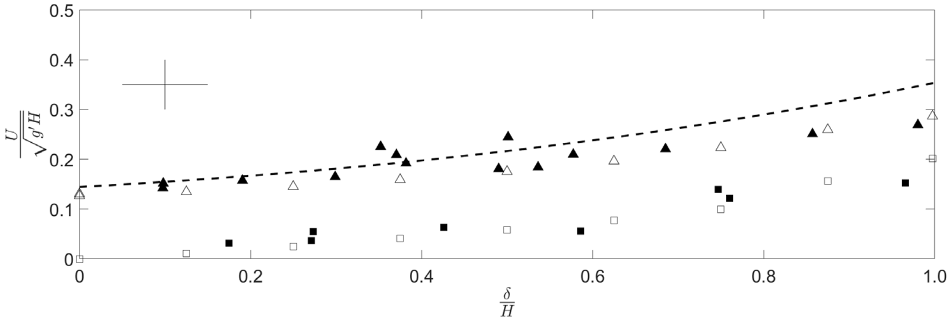

Figure 5.7: Non-dimensional internal front speed versus non-dimensional interface thickness. In all cases $\frac{h_{T1}}{H} = 0.5$. Data were obtained from experiments with $\frac{h_{01}}{H} = 1.0$ (triangles) and 0.5 (squares). Open symbols represent DNS data while closed symbols are data points from laboratory experiments. The dashed line is the prediction made by the Yih-type analysis for $\frac{h_{01}}{H} = 1.0$. Representative error bars are as shown.

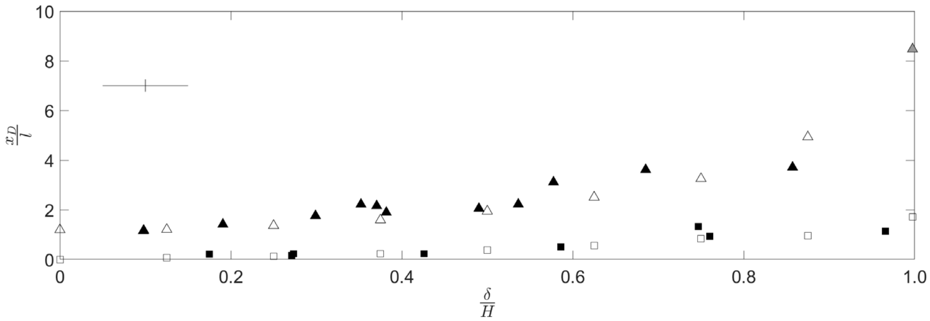

Figure 5.8: Distance of first deceleration of the internal front vs. non-dimensional interface thickness. In all cases $\frac{h_{T1}}{H} = 0.5$. Data include triangles ($\frac{h_{01}}{H} = 1.0$) and squares ($\frac{h_{01}}{H} = 0.5$). Open symbols represent DNS data while closed symbols are data obtained from laboratory experiments. The grey triangle on the right-hand side of the plot represents an experiment where the internal front was stopped by the tank end wall and would have travelled farther in a longer domain. Representative error bars are as shown.

Figure 5.8 shows the horizontal distance, x_D, where the internal front first begins to decelerate and its variation with $\frac{\delta}{H}$. Similar to figure 5.6, we observe that x_D increases with the interface thickness, sharply where $\frac{h_{01}}{H} = 1.0$ and $\frac{\delta}{H} \rightarrow 1$. If we assume that the speed of GC2 varied relatively little with increased interface thickness (as was observed when h_{T1} was decreased) the increase in the speed of the internal front would allow it to travel further before being overtaken by the GC2 front. The triangles ($\frac{h_{01}}{H} = 1.0$) increase more sharply than the squares ($\frac{h_{01}}{H} = 0.5$) as $\frac{\delta}{H} \rightarrow 1$ due to the increased potential energy available for larger h_{01}, which results in faster internal front propagation, and longer propagation distances before deceleration.

Chapter 6

Summary and Conclusion

6.1 Summary

The present study considered the time-dependent flow of gravity currents propagating in a two-layer density-stratified environment in the limiting case where the gravity current and lower ambient layer were of equal density, i.e. $S = 1$. Note that in this study, what would otherwise ($S < 1$) be referred to as the gravity current, i.e. the dense lock fluid, is more appropriately termed the internal bolus, since in our study the boundary (or internal front) between the lock fluid and the lower ambient layer is defined by a difference of passive, not active, scalar. Reserving the term "gravity current" (GC) for circumstances involving a density difference, we refer to GC1 as the flow of dense fluid and GC2 as the flow of the light fluid (both which may include a tailwater in addition to the reservoir fluid – see figure 1.1). In this study, we tracked, using a two-layer shallow water (SW) theory the motion of GC1 and of GC2 where, in the latter case, attention was paid to the period before and after reflection from the back of the lock.

Although the $S = 1$ regime has been previously studied by Ungarish et al. (2014), this thesis expands on this previous investigation in numerous ways. Firstly, and in addition to exploring the post-reflection dynamics of GC2, we track the evolution of the dense lock fluid. This dense lock fluid travels at constant speed over a limited horizontal distance, which is, in turn, an increasing function of h_{01} and δ and a decreasing function of h_{T1}. We also introduce a new, Yih-type analysis (Yih, 1965) which yields an algebraic formula for the speeds of the internal and GC1 fronts. Additionally, we perform laboratory as well as numerical experiments. Finally, we consider thick as well as thin ambient interfaces.

Following the introductory Chapter 1 of this thesis, Chapter 2 outlines the SW theory which will be later compared to experiment. The analysis presented in Chapter 2 is an adaptation of the methods of Ungarish (2009) and Ungarish et al. (2014) to the present investigation. This analysis was only applicable to the experiments that had a thin interface. Following a discussion of the governing system of hyperbolic PDEs and their solution by the method of characteristics, the boundary condition at the gravity current nose is discussed. Note that in the $S = 1$ case three distinct nose types are possible: a subcritical bore (which we termed type 1), a critical bore (type 2), and a rarefaction wave (type 3). Next, specific solution methods are discussed – these are dependent on the GC nose type. Note that some of these had not been encountered in previous work, e.g. when the GC2 nose is of type 1. Finally, the reader is referred to Appendix C for a further discussion of solution methods.

Chapter 3 outlines an original analysis of $S = 1$ gravity currents with thick and thin interfaces. These calculations follow the style of Yih (1965), in which he considers changes in potential and kinetic energy of the dense and light fluids in a lock-exchange scenario, and makes the simplifying assumption that energy is conserved. Both the new thin and thick interface calculations proceed in a similar fashion, considering each layer of fluid in turn. In concert with the thick interface experiments performed in this investigation, the density in the interface is considered to vary linearly between the heavy and light fluids. The thick interface is treated as a separate layer in the calculations. The new calculations result in algebraic expressions for the internal front and GC1 speeds. An additional relation is needed to define the height of GC1 and the internal front – this is achieved by defining, as Yih did, the GC1 height to be the average of h_{01} and h_{T1}. While this Yih-type analysis makes a number of simplifying assumptions, including that the GC1 and GC2 noses are always of type 1, it yields surprisingly good predictions for the speed of the internal front and GC1.

The experimental and post-processing methods are described in Chapter 4. A total of 43 laboratory experiments and 84 direct numerical simulations (DNS) were performed. The fluid domain was 227 cm × 20 cm (× 34 cm wide) with a 35.6 cm long lock in the laboratory experiments and 400 cm × 20 cm with a 40 cm long lock in the majority of the DNS experiments. Approximately one half of these lock-release experiments involved a thin ambient interface (approximately 2 cm in laboratory experiments and vanishingly thin in the DNS experiments), while the interface thickness ranged from 0 to 19.95 cm in the other half of the experiments. The raw data from each experiment consisted either of video taken with a DSLR camera or of analogous DNS images. The experimental images were post-processed and analyzed to determine the speed of the internal front, GC1, and GC2 and height of GC1 and GC2. Additionally, the distance travelled by the internal front during the constant-speed phase of its evolution was measured.

Chapter 5 discusses experimental results, for both thick- and thin-interface experiments. Comparisons between theory and experiment are drawn as outlined in this paragraph and the next. For the thin interface experiments, the internal front speed was found to decrease both with increasing h_{T1} and decreasing h_{01}. This agrees with the findings of Tan et al. (2011) in their study of $S < 1$ gravity currents. By contrast, the GC1 and GC2 front speeds were insensitive to h_{01} (though the heights of both gravity currents increased with h_{01}). Moreover, the GC1 and GC2 front speeds decreased with increasing h_{T1} when $\frac{h_{T1}}{H} > 0.5$. In our study, the distance travelled by the internal front before being arrested by the overtaking GC2 front was found to increase sharply with decreasing h_{T1} and to decrease with h_{01}. In general, the predictions made by our

SW theory and the Yih-type analysis for the internal front speed and the GC1 speed and height corresponded closely to our measurements. Conversely, the front speed and height of GC2 were predicted with less accuracy, in general. Ours is not the first study in which such deviations have been observed. For instance, Longo et al. (2015) also found a discrepancy between SW theory and experiment in the reflected GC2 speeds in a channel with a circular or semi-circular cross-sections. We surmise that the under prediction of the reflected GC2 front speed was due to a mismatch between the location at which the SW prediction was made (i.e. immediately following GC2 reflection) and the location at which GC2 speed was measured (typically 0.5 to 2.5 lock lengths downstream). In between these two points the flow conditions upstream of the GC2 bore changed non-trivially due to dispersion and non-hydrostatic effects. Notwithstanding the above, our SW theory made excellent predictions of the distance travelled downstream by the internal front before being arrested by an overtaking GC2 front (figure 5.6).

For the thick interface experiments, we found an approximate $\frac{U}{\sqrt{g'H}} = 0.2$ increase in the internal front speed as $\frac{\delta}{H}$ varied from 0 to 1 for $\frac{h_{01}}{H} = 0.5, 0.75$, and 1.0. An increase in the distance travelled by the internal front at constant speed before decelerating was also observed. The internal front speed at $\frac{\delta}{H} = 1$ compared favourably to that found in related studies by Ungarish & Huppert (2002) and Maxworthy et al. (2002). Additionally, the Yih-type analysis that was performed for varying δ when $\frac{h_{01}}{H} = 1.0$ was in reasonably good agreement with the experimentally-measured internal front speed.

6.2 Conclusion

In general terms, this investigation resulted in an improved understanding of the behaviour of gravity currents propagating in two-layer ambient environments that include a “tailwater”, i.e. a layer with density equal to the propagating fluid ($S = 1$). In many ways this behaviour is unique. For example, where in $S < 1$ cases the leading edge of the propagating fluid forms a rounded and quite sharply-defined nose that often moves at a higher speed than the upstream fluid, in the present $S = 1$ case the leading edge of the propagating fluid (the internal front) often spans the entire vertical extent of the tailwater and moves at the same speed as the upstream tailwater.

The present study can be linked directly to the previous $S = 1$ data and theory of Ungarish et al. (2014). Furthermore, these new experiments and theory provide a starting point from which to understand the behaviour of the subcritical regime ($0.75 \lesssim S \leq 1$) more generally. While the $S = 1$ behaviour is unique in some ways as mentioned above, the measured parameters also follow smoothly from previous $0.75 \lesssim S \leq 1$ results, such as those of Tan et al. (2011).

The scope of the present research may also be augmented by future work, especially in the realm of thick interface experiments, wherein the height of the ambient interface, h_{T1}, may be varied, and the behaviour of the internal waves generated within the thick ambient interface studied. From a laboratory experimental point of view, this latter task would require the use of more sophisticated measurement techniques e.g. synthetic schlieren (Sutherland et al., 1999; Flynn & Sutherland, 2004) or particle image velocimetry.

Also, while Ungarish (2009) and others have addressed the question of SW theory for ambients with continuous density stratification, we were not able to apply these directly to our study. In particular, we considered the case of thick interfaces that spanned only a portion of the channel depth. To this end, it would be useful to adapt a SW theory to one that makes predictions that apply directly to this thick interface scenario.

Inasmuch as our Yih-type analysis applies to the thick interface scenario where $h_{01} = H$, it would be useful to develop such a theory that applies to $h_{01} < H$. This was attempted, but a satisfactory result was not obtained. Specifically, the complexity of the problem increases substantially when the thick interface forms part of the layer overlying the dense lock fluid, i.e. where $h_{T1} + \delta/2 > h_{01}$.

In more general terms, and acknowledging that $S = 1$ gravity currents may occur in a variety of real-world situations, other experimental geometries may be considered. For instance, oceanic and atmospheric currents may flow up or down sloping terrain or across undulating topography. Axisymmetric gravity currents could also be investigated; these occur in scenarios such as the thunderstorm outflow winds that result from downdrafts spreading horizontally along the Earth's surface. Expanding this study into the non-Boussinesq regime, and considering infinite rather than finite upper layer depths, would be also be useful in studying dam-break and flooding scenarios, extending work by Pritchard & Hogg (2002) among others.

Bibliography

T. B. Benjamin. Gravity currents and related phenomena. *Journal of Fluid Mechanics*, 31(2):209–248, 1968.

D. Bolster, A. Hang, & P. F. Linden. The front speed of intrusions into a continuously stratified medium. *Journal of Fluid Mechanics*, 594:369–377, 2008.

M. R. Flynn & B. R. Sutherland. Intrusive gravity currents and internal gravity wave generation in stratified fluid. *J. Fluid Mech.*, 514:355–383, 2004.

M. R. Flynn, T. Boubarne, & P. F. Linden. The dynamics of steady, partial-depth intrusive gravity currents. *Atmosphere-Ocean*, 46:421–432, 2008.

M. R. Flynn, M. Ungarish, & A. W. Tan. Gravity currents in a two-layer stratified ambient: The theory for the steady-state (front condition) and lock-released flows, and experimental confirmations. *Physics of Fluids*, 24(2):26, Feb 2012.

R. Fulton, D. S. Zrnić, & R. J. Doviak. Initiation of a solitary wave family in the demise of a nocturnal thunderstorm density current. *Journal of the Atmospheric Sciences*, 47(3):319–337, 1990.

J. Y. Holyer & H. E. Huppert. Gravity currents entering a two-layer fluid. *Journal of Fluid Mechanics*, 100(4):739–767, 1980.

H. E. Huppert & J. E. Simpson. The slumping of gravity currents. *Journal of Fluid Mechanics*, 99(4):785–799, 1980.

J. B. Klemp, R. Rotunno, & W. C. Skamarock. On the propagation of internal bores. *Journal of Fluid Mechanics*, 331:81–106, 1997.

P. Kundu, I. Cohen, & D. Dowling. *Fluid Mechanics.* Academic, Berlin, 5th edition, 2012.

S. Longo, M. Ungarish, V. D. Federico, L. Chiapponi, & A. Maranzoni. The propagation of gravity currents in a circular cross-section channel: experiments and theory. *Journal of Fluid Mechanics*, 764:513–537, 2015.

B. D. Maurer, D. T. Bolster, & P. Linden. Intrusive gravity currents between two stably stratified fluids. *Journal of Fluid Mechanics*, 647:53–69, 2010.

T. Maxworthy, J. S. J. E. Leilich, J. E. Simpson, & E. H. Meiburg. The propagation of a gravity current into a linearly stratified fluid. *Journal of Fluid Mechanics*, 453: 371–394, 2002.

A. Mehta, B. R. Sutherland, & P. J. Kyba. Interfacial gravity currents: Part II - wave excitation. *Physics of Fluids*, 14:3558–3569, 2002.

G. Oster. Density gradients. *Scientific American*, 213(2):70–79, 1965.

J. Patterson, P. Hamblin, & J. Imberger. Classification and dynamic simulation of the vertical density structure of lakes 1. *Limnology and oceanography*, 29(4):845–861, 1984.

D. Pritchard & A. J. Hogg. On sediment transport under dam-break flow. *Journal of Fluid Mechanics*, 473:265–274, 2002.

J. W. Rottman & J. E. Simpson. Gravity currents produced by instantaneous releases of a heavy fluid in a rectangular channel. *Journal of Fluid Mechanics*, 135:95–110, 1983.

J. Shin, S. B. Dalziel, & P. F. Linden. Gravity currents produced by lock exchange. *Journal of Fluid Mechanics*, 521:1–34, 2004.

J. E. Simpson. *Gravity Currents: In the Environment and the Laboratory.* Cambridge university press, 1999.

B. R. Sutherland & J. T. Nault. Intrusive gravity currents propagating along thin and thick interfaces. *Journal of Fluid Mechanics*, 586:109–118, 2007.

B. R. Sutherland, S. B. Dalziel, G. O. Hughes, & P. F. Linden. Visualisation and measurement of internal waves by "synthetic schlieren". Part 1: Vertically oscillating cylinder. *J. Fluid Mech.*, 390:93–126, 1999.

B. R. Sutherland, P. J. Kyba, & M. R. Flynn. Intrusive gravity currents in two-layer fluids. *Journal of Fluid Mechanics*, 514:327–353, 2004.

A. W. Tan, D. S. Nobes, B. A. Fleck, & M. R. Flynn. Gravity currents in two-layer stratified media. *Environmental Fluid Mechanics*, 11(2):203–223, 2011.

J. R. Taylor. *Numerical simulations of the stratified oceanic bottom boundary layer.* PhD thesis, Jan 1, 2008.

M. Ungarish. *An Introduction to Gravity Currents and Intrusions.* Chapman and Hall/CRC, 2009.

M. Ungarish & H. E. Huppert. On gravity currents propagating at the base of a stratified ambient. *Journal of Fluid Mechanics*, 458:283–301, 2002.

M. Ungarish, Z. Borden, & E. Meiburg. Gravity currents with tailwaters in Boussinesq and non-Boussinesq systems: two-layer shallow-water dam-break solutions and Navier–Stokes simulations. *Environmental Fluid Mechanics*, 14(2):451–470, 2014.

T. von Kármán. The engineer grapples with nonlinear problems. *Bulletin of the American Mathematical Society*, 46(8):615–683, 1940.

B. L. White & K. R. Helfrich. A general description of a gravity current front propagating in a two-layer stratified fluid. *Journal of Fluid Mechanics*, 711:545–575, 2012.

I. Wood & J. Simpson. Jumps in layered miscible fluids. *Journal of Fluid Mechanics*, 140:329–342, 1984.

C.-S. Yih. *Dynamics of Nonhomogeneous Fluids.* MacMillan Co., New York, 1965.

Appendix A

Summary of Experiments

A summary of the data relevant to our laboratory and DNS experiments is provided in tables A.1 and A.2, respectively.

A.1 Laboratory Experiments

Table A.1: Laboratory experimental data (cgs units). All lock lengths were 35.6 cm. We did not attempt to measure V_{N1} and V_{N2} for the thick interface experiments.

No.	H	h_{01}	h_{T1}	δ	ρ_1	ρ_2	U	V_{N1}	V_{N2}	x_D
1	20.5	20.0	10.2	thin	1.04537	0.99900	4.25	14.46	11.76	40.9
2	20.1	19.9	15.1	thin	1.04087	0.99880	1.43	11.03	8.62	12.1
3	20.6	20.0	4.8	thin	1.04245	0.99875	9.06	13.18	13.14	152.4
4	20.4	20.0	7.4	thin	1.04106	0.99879	6.36	14.37	11.83	65.9
5	20.3	20.0	12.7	thin	1.04010	0.99880	2.34	12.27	10.08	23.5
6	20.2	15.2	10.0	thin	1.04110	0.99895	3.16	11.99	9.94	26.8
7	20.4	20.0	10.0	thin	1.03880	0.99884	4.21	13.47	10.63	41.7
8	20.4	15.3	5.0	thin	1.03872	0.99893	8.06	13.38	11.00	103.2
9	20.3	15.3	7.5	thin	1.03875	0.99872	5.81	12.49	9.61	46.3
10	20.5	15.4	2.5	thin	1.04100	0.99875	11.71	12.95	12.33	124.8
11	20.1	15.1	12.6	thin	1.04020	0.99875	1.48	11.68	9.62	15.9
12	20.2	10.1	7.4	thin	1.04220	0.99875	2.68	13.20	10.17	16.3
13	20.7	10.4	2.6	thin	1.04185	0.99893	11.15	12.83	11.18	110.1
14	20.2	10.1	5.1	thin	1.03919	0.99860	4.76	12.73	11.80	38.3
15	20.5	20.0	10.3	10.3	1.04525	0.99900	7.29	-	-	154.8
16	20.3	19.9	9.3	7.2	1.0382	1.0010	6.02	-	-	79.1
17	20.4	20.0	10.0	7.6	1.0463	1.0007	6.17	-	-	76.9
18	20.4	20.1	9.7	11.8	1.0381	0.9990	5.76	-	-	110.9
19	20.4	20.0	10.6	14.0	1.0374	0.9996	5.96	-	-	128.8
20	20.4	20.0	10	20.0	1.0884	1.0520	6.96	-	-	191.4

Continued on next page

Table A.1 – continued from previous page

No.	H	h_{01}	h_{T1}	δ	ρ_1	ρ_2	U	V_{N1}	V_{N2}	x_D
21	20.4	20.0	10	6.1	1.0374	1.0010	4.37	-	-	62.7
22	20.2	15.2	10.3	6.3	1.0370	0.9985	3.68	-	-	34.6
23	20.2	15.2	10.1	6.8	1.0335	1.0008	4.73	-	-	46.3
24	20.4	12.0	10.0	15.2	1.0352	1.0004	3.62	-	-	47.3
25	20.4	20.0	10.3	10.0	1.0373	0.9983	4.96	-	-	73.1
26	20.4	20.0	10.2	3.9	1.0390	0.9984	4.40	-	-	50.4
27	20.2	15.2	10.1	10.7	1.0374	0.9985	4.39	-	-	51.9
28	20.2	15.2	10.1	2.3	1.0380	0.9985	3.60	-	-	29.0
29	20.4	15.2	10.1	13.4	1.0360	0.9999	4.78	-	-	69.0
30	20.2	10.6	10.1	15.4	1.0366	0.9988	3.27	-	-	33.2
31	20.0	10.4	10.0	11.7	1.0367	0.9982	1.51	-	-	18.4
32	20.0	9.8	9.4	3.5	1.0381	0.9983	0.86	-	-	7.6
33	20.0	9.9	9.6	5.4	1.0395	0.9984	1.02	-	-	5.4
34	20.4	20.0	9.5	7.8	1.0365	0.9982	5.22	-	-	67.4
35	20.2	15.2	9.5	7.3	1.0358	1.0001	4.19	-	-	39.4
36	20.2	15.2	10.1	19.5	1.0682	1.0315	6.59	-	-	173.8
37	20.2	15.2	10.0	17.0	1.0684	1.0381	5.74	-	-	133.0
38	20.1	10.1	10.0	19.4	1.0685	1.0334	3.88	-	-	40.5
39	20.3	20.0	10.2	17.4	1.0911	1.0561	6.34	-	-	132.2
40	20.4	20.0	10.2	10.9	1.0394	0.9986	5.16	-	-	79.2
41	20.2	15.2	10.1	8.2	1.0381	0.9982	4.15	-	-	39.7
42	20.0	10.0	10.0	5.5	1.0383	0.9987	1.50	-	-	8.1
43	20.0	10.0	10.0	8.5	1.0363	0.9986	1.69	-	-	8.4

A.2 DNS Experiments

Table A.2: DNS experimental data (cgs units). In all cases $H = 20\,\text{cm}$, $\rho_1 = 1.02\,\text{g/cm}^3$, and $\rho_2 = 1.00\,\text{g/cm}^3$. We did not attempt to measure V_{N1} and V_{N2} for the thick interface experiments.

Case	l_1	$l_1 + l_2$	h_{01}	h_{T1}	δ	U	V_{N1}	V_{N2}	x_D
246	40	400	20	10	0	2.49	9.82	8.31	47.8
247	40	400	20	5	0	5.49	9.87	9.34	133.8
248	40	400	20	15	0	0.79	7.91	6.08	13.1
249	40	400	20	2.5	0	8.20	9.58	9.05	332.8
255	40	400	20	6.64	0	4.31	10.02	8.35	94.2
501	40	400	15	10	0	1.89	9.82	9.11	21.8
502	40	400	15	7.5	0	3.28	10.02	8.96	49.8

Continued on next page

Table A.2 – continued from previous page

Case	l_1	$l_1 + l_2$	h_{01}	h_{T1}	δ	U	V_{N1}	V_{N2}	x_D
503	40	400	15	5	0	5.11	9.85	10.43	90.9
504	40	400	15	2.5	0	8.09	9.54	11.56	293.2
505	40	400	15	12.5	0	0.81	9.02	9.65	8.6
514	40	400	15	13.75	0	0.38	8.51	7.20	3.9
506	40	400	10	2.5	0	7.19	9.35	7.76	109.8
507	40	400	10	5	0	3.28	9.73	8.58	40.8
508	40	400	10	7.5	0	1.33	9.93	7.06	11.5
509	40	400	10	10	0	0	-	-	0
510	40	400	20	17.5	0	0.28	6.16	4.11	5.6
511	40	400	20	7.5	0	3.79	10.25	8.47	74.0
512	40	400	20	12.5	0	1.55	9.30	7.62	24.7
513	40	400	20	13.3	0	1.30	8.93	7.29	20.8
515	40	400	17.5	2.5	0	8.06	9.76	9.39	335.6
516	40	400	17.5	5	0	5.37	10.06	9.34	118.2
517	40	400	17.5	7.5	0	3.70	10.24	8.84	58.8
518	40	400	17.5	10	0	2.45	10.01	8.16	33.0
519	40	400	17.5	12.5	0	1.40	9.30	7.57	17.4
520	40	400	17.5	15	0	0.59	7.91	6.48	7.2
521	40	400	12.5	5	0	4.29	9.95	7.59	56.6
522	40	400	12.5	2.5	0	7.95	9.63	7.79	208.6
523	40	400	12.5	7.5	0	2.49	10.16	7.28	27.1
524	40	400	12.5	10	0	1.01	9.93	7.03	8.8
525	40	400	20	10	5	2.85	7.74	-	54.5
526	40	400	20	10	10	3.44	-	-	77.8
527	40	400	20	10	15	4.38	-	-	130.1
528	40	400	20	10	19.95	5.62	-	-	338.9
529	40	400	20	10	2.5	2.64	-	-	48.3
530	40	400	20	10	7.5	3.12	-	-	63.7
531	40	400	20	10	12.5	3.85	-	-	100.2
532	40	400	20	10	17.5	5.09	-	-	197.3
533	40	400	15	10	2.5	2.10	-	-	22.5
534	40	400	15	10	5	2.26	-	-	26.6
535	40	400	15	10	7.5	2.73	-	-	30.5
536	40	400	15	10	10	3.03	-	-	37.9
537	40	400	15	10	12.5	3.47	-	-	48.3
538	40	400	15	10	15	4.02	-	-	73.3
539	40	400	15	10	17.5	4.84	-	-	136.2
540	40	400	15	10	19.95	5.50	-	-	273.1
541	40	400	10	10	2.5	0.21	-	-	2.8
542	40	400	10	10	5	0.48	-	-	5.1

Continued on next page

Table A.2 – continued from previous page

Case	l_1	$l_1 + l_2$	h_{01}	h_{T1}	δ	U	V_{N1}	V_{N2}	x_D
543	40	400	10	10	7.5	0.80	-	-	9.0
544	40	400	10	10	10	1.14	-	-	14.9
545	40	400	10	10	12.5	1.52	-	-	22.2
546	40	400	10	10	15	1.95	-	-	33.7
547	40	400	10	10	17.5	3.06	-	-	38.0
548	40	400	10	10	19.95	3.95	-	-	68.3
549	120	400	15	10	0	1.95	9.85	8.34	68.3
550	120	400	15	7.5	0	3.93	10.15	8.67	73.4
551	120	400	10	7.5	0	1.45	9.80	8.34	45.8
552	120	400	10	5	0	3.95	9.69	8.85	134.5
553	80	400	15	5	0	5.94	9.95	7.60	145.0
554	80	400	17.5	5	0	5.65	9.75	8.95	244.4
555	80	400	17.5	7.5	0	4.00	9.81	8.39	103.6
556	80	400	17.5	10	0	2.57	9.45	7.92	71.2
557	80	400	17.5	2.5	0	8.22	9.54	8.56	303.4
558	80	400	17.5	12.5	0	1.44	8.52	7.37	37.2
559	80	400	17.5	15	0	0.58	7.83	6.45	15.5
560	80	400	12.5	2.5	0	8.23	9.54	-	239.3
561	80	400	12.5	5	0	5.21	9.88	9.54	90.3
562	80	400	12.5	7.5	0	2.57	10.05	8.17	59.8
563	80	400	12.5	10	0	1.09	9.81	-	23.1
564	40	400	15	1	0	9.40	9.58	9.61	-
565	40	400	12.5	1	0	8.90	9.31	8.82	-
566	40	400	10	1	0	8.27	8.98	8.09	-
567	40	400	15	0	0	8.57	8.57	-	-
568	40	400	12.5	0	0	8.43	8.43	-	-
569	40	400	10	0	0	7.71	7.79	-	-
570	40	400	17.5	0	0	8.74	-	-	216.4
571	40	400	20	0	0	8.67	8.67	-	248.1
572	40	400	17.5	1	0	9.37	9.31	8.95	358.6
573	40	400	20	1	0	9.40	9.57	8.95	359.6
578	80	600	15	5	0	5.11	9.75	9.54	193.0
579	80	600	17.5	5	0	5.53	9.95	9.28	248.0
580	80	600	17.5	2.5	0	8.54	9.46	-	506.0
581	80	600	12.5	2.5	0	8.46	9.38	-	477.0
582	71.2	400	20	10	0	2.56	10.01	7.80	145.5
583	35.6	400	20	10	0	2.52	10.03	8.18	73.04
584	35.6	400	20	10	0	7.74	9.64	9.38	219.5

Appendix B

Preparation of the Laboratory Experiments

Laboratory experiments with a thin interface ($\delta \simeq 2\,\mathrm{cm}$) were prepared by first adding a layer of salt water to a depth $> h_{T1}$ to the experimental tank with the lock gate in the up position. In cases where $h_{01} < H$, a layer of fresh water (of depth $20\,\mathrm{cm}-h_{01}$) dyed orange with food colouring was layered on top of the salt water layer using a sponge float to minimize interfacial mixing. The lock gate was then lowered to a depth of approximately 1 cm from the bottom of the tank. More (orange-dyed) fresh water was then added to the ambient side of the tank. The resulting imbalance of hydrostatic pressures between the outside and inside of the lock pushed down the ambient interface and up the interface inside the lock. Addition of dyed fresh water was continued until the fluid in the lock reached a total depth of 20.0 cm and, simultaneously, h_{01} reached its desired value. Blue food colouring was then injected into the lower, dense, lock fluid layer using a syringe with a long needle. Note that the above technique allowed for an almost exact match between the densities of reservoir 1 and of tongue 1. In the simpler cases where $h_{01} = H$, the procedure was identical to the above except that no orange-dyed fresh water was added before the lock gate was lowered to within 1 cm of the tank bottom. All the fresh water was added after this step. Also, a syringe and needle were not required to add the blue dye to the lock fluid.

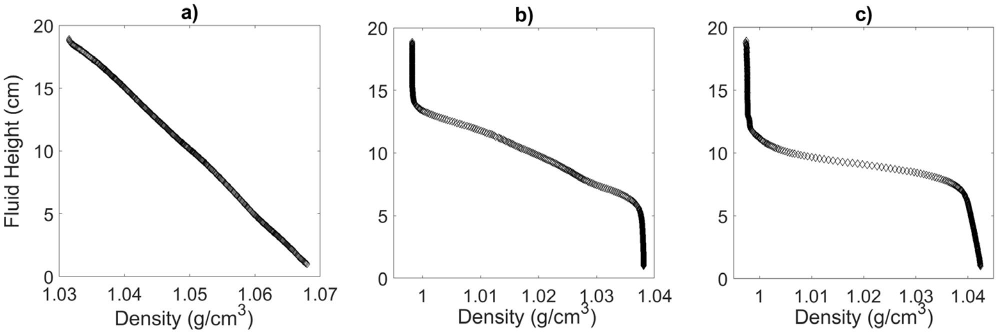

Figure B.1: Examples of ambient interface density profiles as measured by the conductivity probe. Shown is the profile from laboratory experiment 36 (a), which is typical of a thick interface experiment, the profile from laboratory experiment 41 (b), which is typical of a medium interface experiment, and the profile in experiment 28 (c), which is typical of an experiment with a thin interface.

Laboratory experiments with thick interfaces were prepared using one of three methods. Examples of density proflies measured with the conductivity probe are shown in figure B.1. For interfaces ranging in thickness from 2-10 cm an intrusive gravity current, such as those described in Mehta, Sutherland & Kyba (2002), was used. This technique involved first filling the tank and lock as for a thin interface experiment. A second lock gate was installed at an appropriate distance from the far tank wall, and after filling the tank, this second lock gate was lowered. The salt and fresh water in this secondary lock were then mixed, the secondary lock was released, and the resulting intrusive gravity current propagated through the ambient region of the tank. In turn, this led to a nontrivial broadening of the ambient interface. The main lock-release experiment was conducted a minimum of 20 minutes later. To keep the density variation within the ambient interface as linear as possible, intrusions could also be released in sequence, where the second lock gate, though fixed in terms of its downstream location, was raised and lowered several times over with complete mixing of the secondary lock fluid occurring prior to each release of the secondary lock.

For interfaces 7-15 cm thick, a lock exchange of the type described by Shin et al. (2004) was instead performed. This technique involved installing a second lock gate at the approximate midpoint of the ambient region of the tank, then filling one side with salt water and the other side with fresh water. The fresh water was then dyed orange with food colouring. To produce an ambient interface having an approximately linear density profile, the second lock gate was raised in a stepwise fashion, approximately 1 cm at a time. Through this process was produced a rising plume of light fluid that propagated along the top of the dense fluid, while a dense gravity current propagated along the base of the light fluid. Repetition of this procedure eventually produced a layer of continuous stratification throughout the tank.

For interface thicknesses of 15-20 cm the double-bucket technique of Oster (1965) was used. We reserved the use of the double-bucket technique to the case of the thickest interfaces because the technique was limited in the overall density difference, $\rho_1 - \rho_2$, that it could produce compared to the other two techniques.

When $h_{01} < h_{T1} + \delta/2$, the upper part of the thick interface had to appear inside and outside of the lock. To achieve this, the intrusion and double-bucket techniques began by filling the tank with salt water to a volume $\geq l_1 w h_{01}$ (where w is the tank width), after which the remaining combination of salt and fresh water was added as required by the technique in question. This resulted in an overfilled tank having a fluid depth of > 20 cm. The main lock gate was then lowered to within 1 cm of the tank bottom and an appropriate volume of lock fluid from just below the thick interface was removed by siphon. Simultaneously, lower layer fluid from outside of the lock flowed into the lock. This process continued until the depth, h_{01}, of reservoir 1 reached the desired value.

In the case where $h_{01} < h_{T1} + \delta/2$ and lock-exchange was being used to thicken the ambient interface, the second lock gate was placed at a location that resulted in a greater initial volume of salt water than fresh water. Thus, following removal of the second lock gate, the resulting ambient interface was at a greater height than that required for the experiment, which also resulted in an overfilled tank. The primary lock gate was then raised to less than 1 cm from the tank bottom, and fluid was siphoned from the lock as described in the previous paragraph. The hydrostatic balance maintained between the lock and ambient sides of the tank during siphoning resulted in a steady decrease in H, h_{T1}, and h_{01}. As before, siphoning was terminated once this trio of variables achieved their desired values and $H_{\text{lock}} = 20.0\,\text{cm}$.

Appendix C

Additional Solution Methods for the Shallow Water Model

As described in §2.3.1, and in Ungarish et al. (2014) when there is one type 3 nose, (2.3) can be integrated along a characteristic starting from the undisturbed fluid bordering the type 3 nose; if the type 3 nose is associated with GC2, then the initial height and speed are chosen as $h_{\text{initial}_1} = 1$ and $u_{\text{initial}_1} = 0$ and integration is along a c_+ characteristic. The solution of (2.3) is then used to obtain characteristic speed spectra $c_\pm(u, h)$ from (2.4). The range of values for h are used to derive a spectrum of $V_{N1}(h)$ using (2.9) and (2.10). For this purpose, $a = h/H$ and $h_{N1} = h$. Finally, $u(h)$ is used to obtain a second spectrum of $V_{N1}(h)$, this time using (2.8) with $u_{N1} = u$ (and, again, $h_{N1} = h$).

With the above speeds to hand, a composite graph may be constructed as in figure C.1. We first consider the intersection point of the two curves labelled as V_{N1}. If their intersection lies between the $c_+(h)$ and the $c_-(h)$ curves then the solution is valid and the GC1 nose is of type 1, with height and speed determined by the aforementioned intersection point. This is the scenario that figure C.1 illustrates. If, instead, the intersection of the two $V_{Ni}(h)$ curves lies above the $c_+(h)$ curve or below the $c_-(h)$

curve, the GC1 nose can be assumed to be of type 2. However, this scenario was never encountered in this investigation.

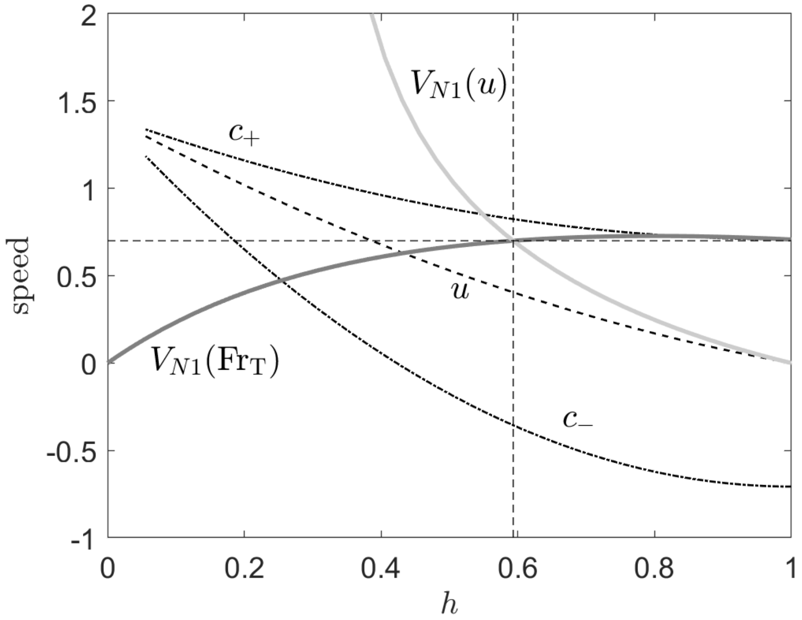

Figure C.1: Sample composite graph showing the variation of u, $c_\pm$, and V_{N1} with h. $V_{N1}(u)$ and $V_{N1}(\mathrm{Fr_T})$ are respectively obtained by applying the solution of (3) into (8) and (9)/(10). The non-dimensional initial conditions are $H = 2.00$ and $b = 0.125$, leading to a type 3 GC2 nose. The height and speed of the GC1 nose are specified by the intersection of the two V_{N1} curves. Because $c_-(h_{N1}) < V_{N1}(h_{N1}) < c_+(h_{N1})$ the GC1 nose is of type 1.

In the case when GC1 is a type 3 nose (instead of GC2), a solution for the GC2 nose can be obtained by inverting the experimental geometry and proceeding as above. Alternately, one may derive a solution by integrating (2.3) along a c_- characteristic having as initial conditions $h_{\mathrm{initial}_2} = h_{T1}$ and $u_{\mathrm{initial}_2} = 0$. Solving along the c_- characteristic implies that $h \in [h_{T1}, 1]$.

In the case when neither GC1 nor GC2 has a nose of type 3, the method described in §2.3.2 is used. First it is assumed that both GC1 and GC2 have a nose of type 2. As a result, (2.3) is integrated twice: both forward along a c_+ characteristic and backward along a c_- characteristic. The initial height to use for the integrations is determined using (5.38) from Ungarish (2009): h_{N1} and h_{N2} are determined then the initial heights are $h_{\text{initial}_1} = h_{N1}$ and $h_{\text{initial}_2} = H - h_{N2}$ and speeds are as shown in figure 2.2. The intersection of the two resulting $u(h)$ curves gives the height and speed of the dense fluid core.

As further described in §2.3.2, when the two curves do not intersect it is because either GC1 or GC2 is of type 1. In this case, (2.3) is still integrated twice, but one of the bores is weakened, i.e. h_{initial_1} must be increased or h_{initial_2} must be decreased (and $u_{\text{initial}_\text{i}}$ follows from continuity arguments). Figure C.2 shows an example solution where the GC1 nose is of type 2 while the GC2 nose is of type 1.

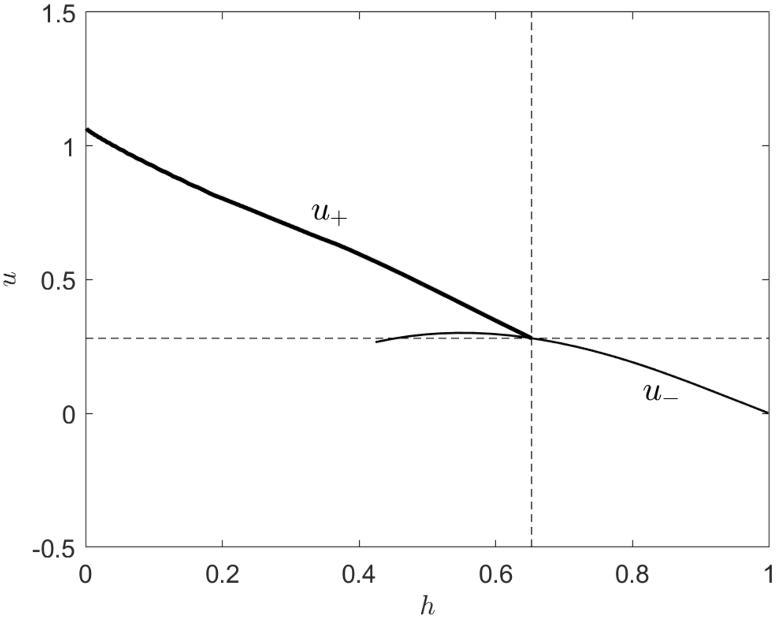

Figure C.2: Sample composite graph of $u(h)$ used when the GC1 nose is of type 2 while the GC2 nose is of type 1. The curves were obtained by integrating (2.3) both forward along a c_+ characteristic (thick line) and backward along a c_- characteristic (thin). The intersection indicates the height and speed of the fluid core between the bores. The parameters are $H = 1$ and $h_{T1} = 0.202$. h_{initial_2} is obtained by reducing the height calculated by (5.38) from Ungarish (2009) by 0.00014 while h_{initial_1} is obtained directly from (5.38).

Appendix D

Comparison of Gravity Current Shapes – SW Theory vs. Experiments

Here, we explore the correspondence between experimental gravity currents and those predicted by SW theory. Before presenting this comparison in full, figure D.1 shows DNS images and gives different examples of gravity current (GC1) shape for each of the three predicted nose types (see §2.2). The examples in the top row, which are predicted to be bores of type 1, tend to have relatively steep frontal slope (especially panel a). Conversely, GC1 examples of the type 3 rarefaction/long wave (bottom row) exhibit a frontal surface of nearly constant and relatively gentle slope. Type 2 critical bores (middle row) tend to be a mixture of type 1 and 3, with both a steep and a gentle slope evident, especially in panel d.

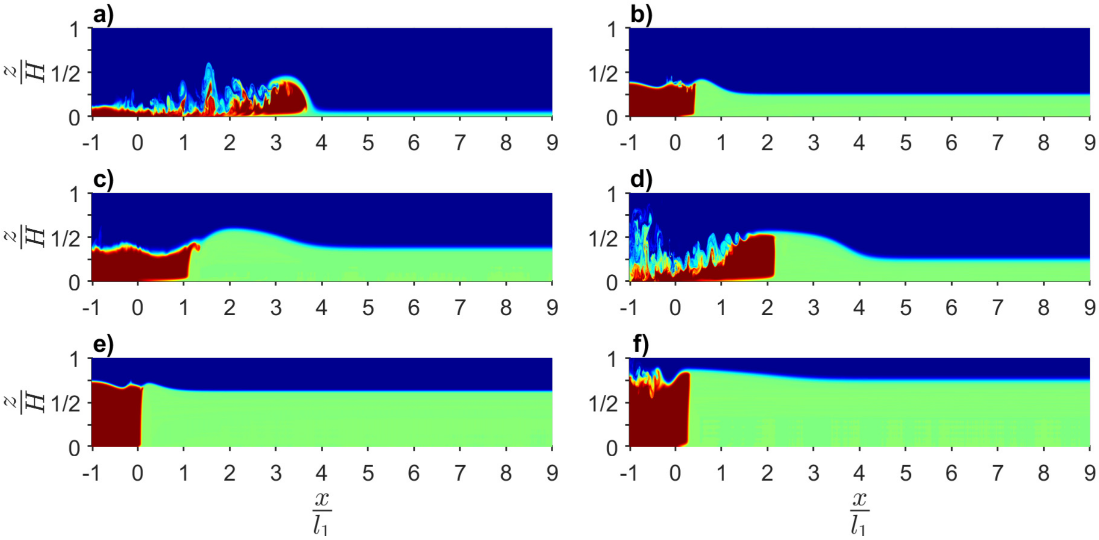

Figure D.1: DNS examples of GC1 noses, grouped by the nose type from SW theory. Each row features two examples of the bore type. Shown are type 1 subcritical bores (a - case 564, and b - case 507), type 2 critical bores (c - case 502, and d - case 247) and type 3 rarefaction/long waves (e - case 505, and f - case 248).

SW results were also used to predict specific gravity current shapes and postions, based on predicted speeds and distances travelled after lock release. These predicted shapes and positions were overlayed on the corresponding laboratory images, and are shown in Figure D.2. Also shown in this figure are the predicted internal front positions. The top panel features a type 1 subcritical bore, which is predicted as a jump just ahead of the bore in the laboratory image. The observed mismatch is due to a slight overprediction of GC1 speed (Fr = 0.443 measured vs. 0.495 SW). In the middle panel a type 2 critical bore is predicted, which includes both a jump and a sloping surface. Also evident is the reflected GC2 bore trailing the internal front. Finally, the bottom panel displays a predicted type 3 rarefaction wave. Here, the correspondence between the predicted position and shape of the two GCs as well as the internal front is excellent. Note that the reflected GC2 bore in the middle and bottom panels is of type 1.

Type 1 – Subcritical Bore

Type 2 – Critical Bore

Type 3 – Rarefaction Wave

Figure D.2: Predicted shape and position of GC1, GC2, (black lines) and the internal front (blue line) overlaid on images from laboratory experiments. Displayed are a GC1s with a predicted type 1 (top), type 2 (middle), and type 3 (bottom) nose. The middle and bottom panels also feature the reflected GC2 nose, which is of type 1 in both cases.

Also shown in the three panels of figure D.2 are the predicted positions of the internal front (vertical blue lines). Generally good agreement with the SW model is seen except in the case of the top panel. Here the internal front forms the (leaky) core of a solitary wave-like GC1, causing it to lead the analogue SW prediction. The internal front's speed is under-predicted by the SW model (Fr = 0.385 measured vs. 0.286 SW).